CHAPTER

11

Observations and Models of Dynamic Topography: Current Status and Future Directions

D.R. Davies[a], *S. Ghelichkhan*[a], *M.J. Hoggard*[a], *A.P. Valentine*[b], *and F.D. Richards*[c]

[a]Research School of Earth Sciences, The Australian National University, Acton, ACT, Australia
[b]Department of Earth Sciences, Durham University, Lower Mountjoy, Durham, United Kingdom
[c]Department of Earth Science and Engineering, Imperial College London, South Kensington, London, United Kingdom

1. Introduction

Earth's surface topography is a product of competition between internal and external processes: some that act to increase elevation, such as mountain building, and others that reduce it, for example, through extension or erosion. Although much of Earth's topography is supported by *isostasy*, being controlled by variations in thickness and density within the crust and lithosphere, a substantial proportion arises as a result of forces exerted by vigorous convection within the underlying mantle (e.g., Braun, 2010; Davies, 1988; Davies et al., 2019; Eakin and Lithgow-Bertelloni, 2018; Hager and Richards, 1989; Hoggard et al., 2016; Parsons and Daly, 1983; Pekeris, 1935). This so-called *dynamic topography* is transient, varying both spatially and temporally in response to underlying mantle flow. As such, it directly connects the evolution of surface environments to Earth's deep interior.

Dynamic topography plays a key role in a diverse range of processes, including sea-level change and continental flooding (e.g., Gurnis, 1993; Mitrovica et al., 1989; Moucha et al., 2008), Earth's gravitational expression (e.g., Colli et al., 2016; Hager, 1984; Hager and Richards, 1989), sedimentary stratigraphy (e.g., Burgess and Gurnis, 1995; Czarnota et al., 2013; Petersen et al., 2010), landscape and shoreline evolution (e.g., Richards et al., 2016; Roberts and White, 2010; Sandiford, 2007; Shephard et al., 2010), oceanic circulation patterns (e.g., Parnell-Turner et al., 2015; Poore et al., 2006, 2009), and ice sheet stability (e.g., Austermann et al., 2015). Despite considerable advances across a number of observational, theoretical,

and computational studies (e.g., Conrad and Husson, 2009; Conrad et al., 2004; Faccenna et al., 2019; Ghelichkhan et al., 2021; Guerri et al., 2016; Gurnis, 1993; Gurnis et al., 2000; Hoggard et al., 2016; Lithgow-Bertelloni and Silver, 1998; Mitrovica et al., 1989; Moucha et al., 2008; Steinberger, 2016; Watkins and Conrad, 2018; White and Lovell, 1997), our understanding of dynamic topography remains incomplete, with ongoing uncertainties on the length scales and amplitude at which it manifests, the rates over which it changes, and the mechanisms driving its evolution (e.g., Colli et al., 2016; Davies et al., 2019; Hoggard et al., 2016, 2021; Molnar et al., 2015; Müller et al., 2018a; Rowley et al., 2013; Yang and Gurnis, 2016).

Several attempts have been made to constrain the spatial pattern, wavelength, and amplitude of present-day dynamic topography. There are generally two ways to approach this: (i) estimation of so-called *residual topography*, by removal of the isostatic contribution due to sediments, ice, crust, and lithosphere from the observed topography (e.g., Crough, 1983; Guerri et al., 2016; Hoggard et al., 2017; Kaban et al., 2003; Menard, 1973; Panasyuk and Hager, 2000) or (ii) estimation of the surface deflections arising from mantle flow, through predictive computational modeling (e.g., Colli et al., 2018; Conrad and Husson, 2009; Flament et al., 2013; Ghelichkhan et al., 2021; Hager et al., 1985; Osei Tutu et al., 2018; Ricard et al., 1993; Rubey et al., 2017; Steinberger, 2007; Yang and Gurnis, 2016). Until recently, the results obtained using these two approaches were inconsistent. Most predictive models exhibited peak amplitudes of greater than 2 km, being dominated by broad topographic highs within the Pacific and African domains, separated by a band of topographic lows extending from Antarctica, through the Americas to the Arctic region and broadening beneath the Eurasian continent. Residual topography estimates, on the other hand, showed smaller-scale structure, with key features including lows at the Australian-Antarctic discordance (AAD) and Argentine Basin, and highs under the central and western Pacific Ocean, offshore southern Africa, and the North Atlantic Ocean. Recent research has, however, broadly resolved this long-standing debate, reconciling theoretical model predictions with careful measurements of residual topography from the geological record (e.g., Davies et al., 2019; Hoggard et al., 2016, 2017; Richards et al., 2020b; Valentine and Davies, 2020). These studies reveal that both deep-mantle flow and shallower processes involving the interaction between asthenospheric flow and lithospheric structure are fundamental to generating Earth's dynamic surface response, with deep-mantle flow primarily contributing to dynamic topography at long wavelengths, and shallower processes controlling the shorter wavelength components ($\sim 10^2$–10^3 km), as advocated in seminal studies by, for example, Hager and Richards (1989).

Despite this progress, there remains a fundamental gap in our understanding of dynamic topography: we do not have a clear picture of how it has evolved in space and time, even for the most recent Cenozoic history of our planet. This limitation arises partly due to increasing sparsity of observational constraints back in time, but also because transient uplift and subsidence events lead to periodic erasing and overprinting of the geological record, resulting in complex interpretational challenges (Hoggard et al., 2021). A growing number of modeling studies have attempted to fill this gap (e.g., Flament, 2019; Flament et al., 2013; Ghelichkhan et al., 2021; Liu et al., 2008; Moucha et al., 2008; Müller et al., 2018a; Rubey et al., 2017; Spasojevic and Gurnis, 2012; Spasojevic et al., 2009), with some now able to reproduce long-wavelength ($\sim 10^4$ km) spatial and temporal patterns of dynamic topography that are consistent with first-order geological events, such as the Cretaceous onset and

Paleocene termination of large-scale marine inundation in North America (e.g., Liu et al., 2008; Mitrovica et al., 1989; Spasojevic et al., 2009), the late Tertiary rise of Africa relative to other continents (e.g., Gurnis et al., 2000; Rubey et al., 2017), the Miocene reversal of the Amazon river drainage system (e.g., Shephard et al., 2010), and post-Cretaceous tilting of Australia (e.g., DiCaprio et al., 2011; Ghelichkhan et al., 2021). Other model predictions, however, remain largely at odds with geological constraints, particularly at shorter spatial and temporal scales (e.g., Ball et al., 2021; Green et al., 2018; Gurnis et al., 2020; McLaren et al., 2012; Paul et al., 2014; Sandiford and Quigley, 2009; Wheeler and White, 2002). This major limitation hampers our ability to understand fundamental processes driven by time-dependent interactions between Earth's surface and its interior. As a result, an accurate reconstruction of dynamic topography into the geological past is now regarded as a grand challenge in global geodynamical research.

Here, the aims of our contribution are twofold. First, we attempt to summarize the current understanding of dynamic topography, both at the present day and into the geological past, through a combination of observational constraints and predictions from geodynamical models. Second, we identify important future directions and approaches that will facilitate more accurate reconstructions of dynamic topography. This review is intended to complement a recent review on observational estimates of dynamic topography through space and time by Hoggard et al. (2021). It also complements and builds on an earlier review on observations and models of dynamic topography by Flament et al. (2013), through the integration of more recent material.

The chapter is divided into two parts. In the first part (Section 2), we focus on the present-day dynamic topography, providing a synopsis of efforts to reconcile present-day observational constraints with model predictions. This part allows us to quantify the sensitivity of dynamic topography to different components of the mantle's flow regime for a period where the observational constraints on dynamic topography and mantle flow are more plentiful. In the second part (Section 3), we focus on dynamic topography through the geological past, summarizing time-dependent observational constraints, methods, and predictions from a range of geodynamical models. This synthesis allows us to highlight the strengths and weaknesses of different modeling approaches and to identify a pathway toward improving future reconstructions of dynamic topography through space and time, which we cover in Section 3.4.

2. Present-day dynamic topography

2.1 Observational estimates

Some of the earliest observational estimates of the amplitude and geographic pattern of present-day dynamic topography came from studies of oceanic bathymetry. In the late 1960s, the observed first-order pattern of increasing basement subsidence as a function of lithospheric age was successfully described using models of conductive cooling of a thermal boundary layer (e.g., McKenzie, 1967; Turcotte and Oxburgh, 1967). Nevertheless, localized deviations away from a classical age-depth relationship were quickly identified and mapped in many of the ocean basins. These features became known as *residual depth anomalies* and were thought to be a proxy for dynamic topography (e.g., Menard, 1969, 1973). Later studies further refined these maps and consensus emerged that depth anomalies could be up to ± 1 km in amplitude, across typical wavelengths of 500–2500 km (e.g., Cazenave et al., 1988; Cochran and Talwani, 1977; Crough, 1983).

More recent research has demonstrated that some of the early-identified features are actually

a result of isostatic topography caused by variations in the thickness and density of the sedimentary pile and crust (e.g., Coffin et al., 2006). Modern residual depth analyses attempt to correct observed bathymetry for these isostatic effects, which requires detailed knowledge of local sedimentary and crustal thicknesses (e.g., Crosby et al., 2006; Hillier and Watts, 2005). The most accurate measurements come from active-source marine seismic experiments, and the last decade has seen steady compilation of a global inventory of more than 2000 such measurements (e.g., Czarnota et al., 2013; Hoggard et al., 2017; Winterbourne et al., 2009, 2014).

Careful analyses, including the propagation of uncertainties associated with the sedimentary and crustal isostatic corrections, have yielded the most reliable constraints on present-day dynamic topography to date. In well-resolved regions, such as the South Atlantic passive margins, multiple cycles of residual depth variations have been observed (Winterbourne et al., 2009). These features have amplitudes of ± 1 km, wavelengths of 1000–2500 km, and correlate with free-air gravity anomalies, subplate seismic velocity variations, and geological evidence for uplift and subsidence in the stratigraphy and geomorphology of adjacent continental shelves and their hinterlands (e.g., Al-Hajri et al., 2009; Hoggard et al., 2017; Roberts and White, 2010). Crucially, these features appear to be robust, since their amplitudes are significantly larger than the associated measurement uncertainties. The oceanic residual topography database of Hoggard et al. (2017) is central to the analyses presented in this review: It has underpinned a series of studies into the spectral character of residual topography and its relationship to underlying mantle dynamics (e.g., Davies et al., 2019; Hoggard et al., 2016; Richards et al., 2020b; Steinberger, 2016; Steinberger et al., 2019; Valentine and Davies, 2020; Watkins and Conrad, 2018; Yang and Gurnis, 2016; Yang et al., 2017). Further details of its construction are described in Section 2.2.

In spite of advances in the quality, quantity, and accuracy of analyses, there remain two significant challenges with residual depth datasets. First, the use of an age-depth model curve as a baseline implies that the lithospheric structure everywhere is equivalent to that predicted by the oceanic cooling model. In reality, there will be local differences in the thermal structure of oceanic lithosphere away from this idealized case, such as thinning above mantle plumes or thickening above cold subduction zones, as indicated by seismological studies of lithospheric structure (e.g., Richards et al., 2020a). Thus, there is potentially still a component of oceanic residual depth anomalies that are supported by lithospheric isostasy, and constraining its amplitude is a focus of considerable ongoing research (e.g., Davies et al., 2019; Richards et al., 2020b).

Second, there is an inherent spatial bias in the high-accuracy measurements caused by the distribution of marine seismic experiments (Hoggard et al., 2017). A high density of data is found along many of the passive margins that have been the subject of extensive hydrocarbon exploration. Similarly, academics have performed many of their seismic surveys at sites of particular geological interest, such as around seamounts, igneous plateaus, volcanic hotspots, subduction zones, and other tectonic boundaries including fracture zones and microplates. The centers of the major ocean basins, where much of the more pristine, bona fide oceanic crust appears to be located, are therefore underrepresented in the database. Where they are included, the experiments often date from the early days of marine seismic acquisition in the 1960s and 1970s, when surveying equipment and processing techniques were less sophisticated and precise than they are today. Improving our current understanding of Earth's residual topography field, in particular its spectral properties, requires obtaining estimates of residual topography in these data "gaps" (e.g., Valentine and Davies, 2020).

There are two avenues of research that aim to tackle this spatial bias problem. In the central ocean basins, gridded datasets derived from shiptrack bathymetry and sediment-thickness maps are used to supplement the high-accuracy spot measurements (e.g., Crosby and McKenzie, 2009; Hillier, 2010; Hoggard et al., 2017; Winterbourne et al., 2014). Improving their accuracy necessitates returning to the original constraints used in their construction and coming up with a suitable approach to deal with the crustal correction in the absence of global grids of oceanic crustal thickness. The more substantial data gaps, however, occur in continental interiors, and obtaining residual topography estimates of sufficient accuracy in this setting is a key goal for observational geodynamics (Hoggard et al., 2021). While even early residual topography studies estimated values in continental areas, the greater crustal and lithospheric thicknesses and wider range of lithologies in comparison to oceanic settings results in considerably larger uncertainties (e.g., Guerri et al., 2015; Panasyuk and Hager, 2000). The impact of complex and protracted tectonic histories, melt depletion events in the early Earth, and subsequent metasomatic enrichment, introduces likely density variations at the ~15% level, which, in turn, produce ±1 km shifts in the isostatic corrections: this is equivalent to the amplitude of the dynamic topography signals being studied (e.g., Guerri et al., 2015; Hoggard et al., 2021; Lamb et al., 2020). Attempts are currently being made to reduce these uncertainties using additional observational constraints, such as using local seismic velocities and/or gravity to better constrain continental density structure (e.g., Brocher, 2005; Davis et al., 2012; Guerri et al., 2015; Wang et al., 2022).

2.2 Oceanic residual topography dataset

The oceanic residual topography dataset of Hoggard et al. (2017) consists of two classes of data. The first are those from the sites of active-source seismic experiments (both reflection and wide-angle refraction surveys), and are generally referred to herein as *spot measurements*. The second are *shiptrack measurements*, which are calculated using global grids of bathymetry and sediment thickness. Each class is described in turn below.

2.2.1 Spot measurements

Approximately 2000 high-accuracy spot measurements have been obtained from seismic images of oceanic crust collected using active-source acquisition techniques. Along each of these profiles, the seabed, sediment-basement interface, and, where possible, Moho have been mapped and converted into estimates of water depth, sedimentary, and crustal thickness. Careful processing allows correction for isostatic topography associated with sedimentary loading (including the effects of compaction) and crustal thickness, and age-depth cooling is accounted for using a plate model (Richards et al., 2018). A total of 1160 residual topography observations are obtained in this manner (circles in Fig. 1A), with associated uncertainties (Fig. 1C). We consider these points to be the most robust within the database. A further 870 points (triangles in Fig. 1A) are obtained in a similar manner, but the lack of an imaged Moho prevents application of a crustal correction. These observations must therefore be assumed to be less accurate. To reflect this, Hoggard et al. (2017) increased the uncertainties reported for these data points by 0.2 km, chosen based on the median crustal correction of all the data that does image oceanic Moho. Valentine and Davies (2020) instead replaced this additional 0.2 km component by a correction, $\Delta = 0.08$ km, determined to ensure statistical consistency with the most robust, crustal-corrected data points. The results presented below use this latter approach.

2.2.2 Shiptrack-derived measurements

The database also contains 20,767 measurements derived from global grids. Water depths are taken from the database of Smith and

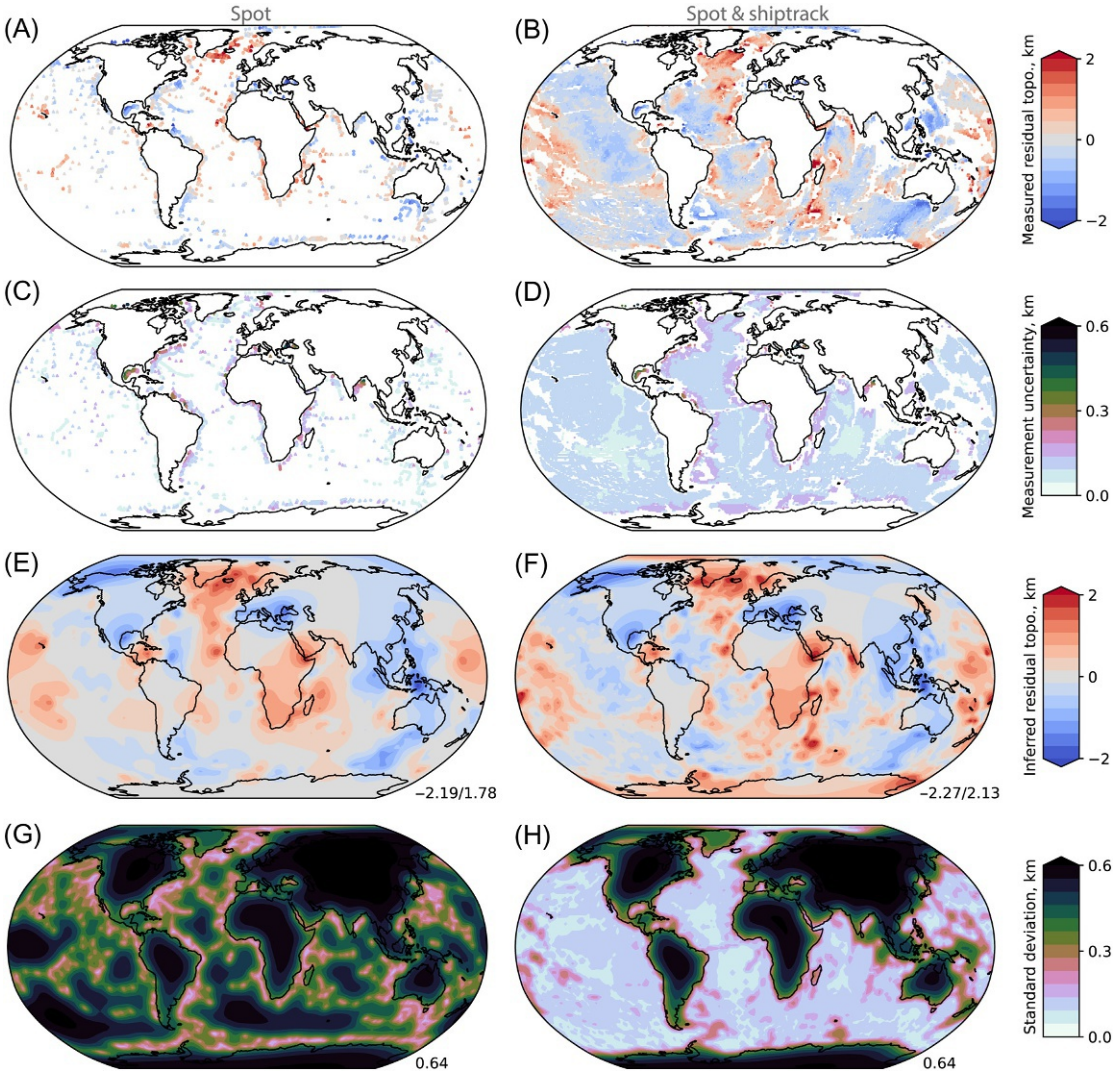

FIG. 1 (A–D) Observational estimates of present-day residual topography from the database of Hoggard et al. (2017). Spot measurements are shown in panel (A), with associated uncertainties in panel (C). High-accuracy measurements that incorporate both crustal and sedimentary corrections are shown as *circles*, with measurements that lack a crustal correction shown as *triangles*. The uncertainty associated with the latter includes an additional 0.08 km that has been determined to bring the robust, crustal-corrected data points into best agreement with the statistical model (see Valentine and Davies, 2020 for further details). Panel (B) shows 20,767 gridded measurements derived from shiptrack bathymetry, where uncertainties depicted in panel (D) now include an additional 0.09 km to reflect the lack of crustal corrections. (E–H) Global water-loaded residual topography determined from observational dataset. Panel (E) shows the posterior mean point-wise estimate of residual topography determined from all spot data, with panel (G) mapping the associated standard deviation. Note that uncertainties rapidly grow with increasing distance from measurement locations and there are large regions (including all continental interiors), where the spot data are uninformative. Panel (F) shows the mean residual topography determined from all available data, including both spot and shiptrack-derived measurements, with associated standard deviation in panel (H). The use of shiptrack-derived data substantially expands the area in which the model is informative. *Color scales* are chosen for consistency with subsequent figures. Minimum and maximum values, or maximum amplitudes, are provided for each map in the lower-right corner.

Sandwell (1997) using only measurements obtained along shiptracks from hull-mounted echosounder systems. The sedimentary correction is based on the sediment-thickness model of Divins (2003), infilled in locations with no data from the global synthesis of Laske and Masters (1997). There are currently no reliable grids of oceanic crustal thickness and so a crustal correction has not been applied. Instead, Hoggard et al. (2017) have attempted to excise anomalous areas of oceanic seafloor (fracture zones, seamounts, and large igneous plateaux) using high-resolution gravity anomalies and bathymetric data. Again, to account for the lack of a crustal correction, they increased the associated measurement uncertainties by 0.2 km, although in the analyses of Valentine and Davies (2020) that are discussed further below, this value was replaced with $\Delta = 0.09$ km, again determined to ensure statistical consistency with information from the most robust spot measurements. Shiptrack-derived data are illustrated in Fig. 1C, with uncertainties in Fig. 1B. These points clearly provide enhanced spatial coverage, but the use of global grids in their construction, which are themselves derived from disparate sources of variable quality, raises the possibility of significant unquantified systematic biases within this portion of the dataset. We therefore regard the shiptrack-derived measurements as being the least robust within our database of oceanic residual topography.

2.3 Global representation of observational dataset

The observation-based dataset illustrated in Fig. 1A–D provides information about residual topography at discrete locations. These locations are unevenly distributed around the globe, and the measurements are associated with significant uncertainty. In order to understand and analyze the patterns of residual topography and their links to underlying mantle dynamics, we need to convert this dataset into a continuous representation, quantifying our knowledge of the topography at any point on Earth's surface. This process requires us to impose assumptions: how should we interpolate between data points and "fill in the gaps"?

One starting point — adopted by Hoggard et al. (2016) and Davies et al. (2019) — is to assume that the topography can be expressed in terms of a finite set of spherical harmonic functions. Using $h(\theta, \varphi)$ to represent the topographic height at latitude θ and longitude φ, we would write

$$h(\theta,\varphi) = \sum_{l=1}^{L} \sum_{m=-l}^{l} a_{lm} \mathcal{Y}_{lm}(\theta,\varphi) \tag{1}$$

where $\mathcal{Y}_{lm}(\theta,\varphi)$ represents a spherical harmonic[a] of degree l and order m, L represents a predetermined maximum spherical harmonic degree for the expansion, and the a_{lm} represent expansion coefficients. To estimate these values, one may set up and solve a regularized least-squares inversion, seeking the vector of coefficients $\mathbf{a}$ that minimizes

$$\phi(\mathbf{a}) = \sum_{i=1}^{N} \frac{1}{\sigma_i^2} \left(d_i - \sum_{l=1}^{L} \sum_{m=-l}^{l} a_{lm} \mathcal{Y}_{lm}(\theta_i \varphi_i) \right)^2 + P(\mathbf{a}) \tag{2}$$

where d_i represents the observation made at location (θ_i, φ_i), and σ_i denotes its corresponding uncertainty. The second term, $P(\mathbf{a})$, represents a regularization function chosen to ensure that ϕ has a well-defined and unique minimum; from a Bayesian viewpoint, it encapsulates our prior

[a] Various definitions and normalization conventions exist for spherical harmonics, and this has been the source of some confusion in the literature on dynamic topography. The results presented herein assume real surface spherical harmonics, as defined in Section B6 of Dahlen and Tromp (1998).

knowledge about the system. Both this regularization function and the maximum spherical harmonic degree L are somewhat arbitrary choices, but each can significantly affect the characteristics of obtained results.

One common choice of regularization function takes the form

$$P(\mathbf{a}) = \frac{1}{2}\sum_{l=1}^{L}\sum_{m=-l}^{l}\left[\alpha^2 + \beta^2 l(l+1)\right]a_{lm}^2 \qquad (3)$$

where α and β are tunable parameters governing the overall power content and roughness, respectively, of the recovered topography. Hoggard et al. (2016) used $L = 30$ and chose values of $\alpha = 20$ and $\beta = 1$, following a series of experiments. This formulation was generalized by Davies et al. (2019), where α and β are instead estimated from the observational data using a hierarchical Bayesian approach developed by Valentine and Sambridge (2018); the values obtained (for the full dataset including both spot- and shiptrack-derived data) were $\alpha = 1.25$ and $\beta = 1.28$. However, this analysis relies heavily on the assumed form of $P(\mathbf{a})$ in Eq. (3). As explained in more detail in Davies et al. (2019), this choice turns out to impose strong constraints on the recovered dynamic topography field and, in particular, on its spectral properties. The assumption is problematic for interpretations and comparisons, as it can be unclear whether features are mandated by the data or are simply an artifact of regularization. To move beyond this limitation, Davies et al. (2019) instead adopted

$$P(\mathbf{a}) = \frac{1}{2}\sum_{l=1}^{L}\sum_{m=-l}^{l}\xi_l a_{lm}^2 \qquad (4)$$

which builds on the concept of automatic relevance determination (ARD) introduced by MacKay (1992). Again, the parameters ξ_l can be estimated from the data, allowing analysis to proceed with a minimum of external assumptions. In order to minimize the effects of spectral leakage (e.g., Trampert and Snieder, 1996), the study of Davies et al. (2019) used $L = 50$ in their inversions, but coefficients above $l = 30$ were subsequently disregarded in their analyses.

A downside to the ARD approach is that it becomes unstable for small datasets, leaving Davies et al. (2019) unable to analyze the high-accuracy spot measurements in isolation. As a result, Valentine and Davies (2020) developed a new framework for analysis of the observational data, replacing the basis-function expansion of Eq. (1) with an assumption that topography can be described by a Gaussian process,

$$h(\theta,\varphi) \sim \mathcal{GP}(\mu(\theta,\varphi), k(\theta,\varphi;\theta',\varphi')) \qquad (5)$$

Here, μ represents a "mean function," quantifying our prior expectations of topography, while the covariance function, k, quantifies our prior assumptions about correlations between the topography at one point (θ, φ) and that at another (θ', φ'). Put another way, k encodes the extent to which a point measurement can be considered to be informative on the surrounding region. Gaussian processes extend the familiar concept of a Gaussian distribution from vector spaces to function spaces, and allow analysis of the observational data to proceed within a rigorous statistical framework; for further details, see, for example, Rasmussen and Williams (2006) or Valentine and Sambridge (2020b). As set out in Valentine and Sambridge (2020a), the Gaussian process framework can be connected to the least-squares inversion used by Hoggard et al. (2016) and Davies et al. (2019): conceptually, it corresponds to allowing $L \to \infty$, applying the transformation $d_i \to d_i - \mu(\theta_i, \varphi_i)$ and choosing

$$P(\mathbf{a}) = \frac{1}{2}\mathbf{a}^{\mathbf{T}}\mathbf{K}^{-\mathbf{1}}\mathbf{a} \qquad (6a)$$

with

$$[\mathbf{K}]_{ij} = \iint_{\Omega^2} \mathcal{Y}_{l_i m_i}(\theta,\varphi)\mathcal{Y}_{l'_j m'_j}(\theta',\varphi')k(\theta,\varphi;\theta',\varphi')\,\mathrm{d}\Omega\,\mathrm{d}\Omega' \qquad (6b)$$

where (l_i, m_i) represent the spherical harmonic degree and order associated with the ith coefficient in the vector $\mathbf{a}$, and where integration is over the surface of the unit sphere. Specifically, Valentine and Davies (2020) assumed a constant mean function,

$$\mu(\theta,\varphi) = \mu_0 \tag{7a}$$

and a Matérn covariance function

$$k(\theta, \varphi; \theta'\varphi') = \sigma_1^2 \frac{2^{1-\nu}}{\Gamma(\nu)} \left(\frac{\sqrt{2\nu}\, d(\theta, \varphi; \theta'\varphi')}{\sigma_2} \right)^{\nu} \times K_\nu \left(\frac{\sqrt{2\nu}\, d(\theta, \varphi; \theta'\varphi')}{\sigma_2} \right) \tag{7b}$$

Here, Γ represents the Gamma function, and K_ν is a modified Bessel function of the second kind. The function d quantifies the distance between any two points on Earth's surface: Valentine and Davies (2020) adopted an epicentral-angle distance metric

$$d(\theta, \varphi; \theta'\varphi') = \arccos \left[\sin\theta \sin\theta' + \cos\theta \cos\theta' \cos(\varphi - \varphi') \right] \tag{7c}$$

The quantities μ_0, σ_1, σ_2, and ν all represent hyperparameters that are tuned to match the characteristics of the data.

Both the least-squares and Gaussian process frameworks enable the construction of a "posterior" (i.e., data-informed) estimate of the dynamic topography field, which we denote $\sim h(\theta,\varphi)$. Following Hoggard et al. (2016), we define the power at degree l within this field as

$$p_l = \sum_{m=-l}^{l} \left[\int_\Omega \sim h(\theta,\varphi) \mathcal{Y}_{lm}(\theta,\varphi)\, \mathrm{d}\Omega \right]^2 \tag{8}$$

If knowledge of $\sim h$ is Gaussian — as is the case for both Gaussian process and Bayesian least-squares results — then our knowledge of p_l is represented by a generalized χ^2 distribution. This formulation has some counterintuitive features: In particular, the most-probable power spectrum is greater than the power spectrum of the mean (i.e., most-probable) dynamic topography field.

The primary advantage of the Gaussian process approach is its mathematical elegance: The only assumptions made are (i) that the topography is representable using a Gaussian process and (ii) that the mean and covariance functions take certain forms. These choices have straightforward physical interpretations, allowing principled choices to be made and any impact on results to be assessed. Beyond this, analysis proceeds without further assumption or approximation.

The Gaussian process model of residual topography from Valentine and Davies (2020), derived from spot measurements only, is mapped in Fig. 1E, with associated uncertainties in Fig. 1G. The spatial pattern is dominated by broad topographic highs within the Pacific, African, and North Atlantic regions, separated by a band of topographic lows that extend from Antarctica, through the Americas to the Arctic, broadening beneath the Eurasian continent and extending south of Australia. Unsurprisingly, given the sparse and uneven data coverage, this model has large uncertainties in many regions of the globe — particularly continental interiors, the Pacific Ocean and the Southern Ocean. This effect must be considered when interpreting the residual topography map.

A repeated analysis, from Valentine and Davies (2020), where the dataset has been extended to include the additional measurements derived from shiptrack bathymetry, is shown in Fig. 1F. It is remarkably consistent with that determined from the spot data alone, despite a significant expansion in spatial coverage of the dataset. Given the 10-fold increase in the number of measurements used to construct the model, finer-scale detail is now evident that was not visible using the spot measurements alone. As expected, the data are informative throughout the oceans with uncertainties markedly reduced (Fig. 1H), but the lack of onshore

data results in significant uncertainties within continental interiors, as noted in Section 2.2.

These residual topography models are next expressed in terms of spherical harmonics, with the resulting power spectra shown in Fig. 2. To represent the (non-Gaussian) uncertainties associated with these spectra, Valentine and Davies (2020) generated power spectra for 100,000 random samples from the posterior residual topography models, and Fig. 2 depicts the ranges spanned by the central 99% and 50% of samples. In general, both datasets tell a similar story: The spectrum of residual topography is relatively flat, peaking at degree-2 (wavelength ~16,000 km), with steadily declining power at shorter length scales. Based on the spot data only, the most-probable model has degree-2 power 0.54 km^2, with power likely in the range 0.47–0.70 km^2 (central 50% of data), although the data could support power up to ~1.12 km^2. By degree-10 (wavelength ~4000 km) and degree-20 (~2000 km), power is likely in the ranges 0.13–0.18 and 0.04–0.06 km^2, respectively. In general, the additional information available when the dataset is expanded to include shiptrack-derived estimates enables a modest reduction in the spectral uncertainty, but does not substantially alter the most-probable power. These results imply that degrees 1–3 account for about 86% of the total power (up to degree 30) in the residual topography field (this drops marginally to about 84% for spot and shiptrack data).

In summary, the analyses of Valentine and Davies (2020) reviewed above: (i) express a preference for 0.54 km^2 of globally water-loaded residual topography power at long wavelength ($l = 2$), likely in the range of 0.47–0.70 km^2, with peak water-loaded amplitudes of 0.74 ± 0.10 km at degrees 1–3; (ii) indicate that spectral power decreases by over an order of magnitude from $l = 2$ to $l = 30$; and (iii) demonstrate the robustness of the low-amplitude, short-wavelength ($l = 15–30$) residual topography component.

2.4 Predictions from simulations of mantle flow

To determine how the observed dynamic topography power spectrum might be related to underlying mantle dynamics, we can investigate predictions of surface deflections that are obtained from simulations of mantle flow. A number of different modeling approaches are available, as reviewed by Flament et al. (2013) and further discussed in Section 3.2. These include time-dependent forward and adjoint simulations of global mantle flow that evolve toward the present day (e.g., Flament, 2019; Flament et al., 2013; Ghelichkhan et al., 2021; Moucha et al., 2008; Müller et al., 2018a; Rubey et al., 2017; Spasojevic and Gurnis, 2012), focused studies that examine the sensitivity of topographic predictions to various controlling parameters (e.g., Arnould et al., 2018; Gurnis, 1993), regional studies that aim to connect dynamic topography to specific aspects of the geological record (e.g., Burgess and Gurnis, 1995; Mitrovica and Jarvis, 1985; Mitrovica et al., 1989; Petersen et al., 2010; Schellart and Spakman, 2015; Uluocak et al., 2021), and global models of instantaneous mantle flow that consider the present-day state of the mantle only (e.g., Conrad and Husson, 2009; Kaban et al., 2003; Panasyuk and Hager, 2000; Ricard et al., 1993; Steinberger, 2007, 2016; Yang and Gurnis, 2016). Due to a comparatively low-computational cost and the multitude of observational constraints that are available at the present day, in particular seismological and geodetic observations constraining the mantle's current thermochemical structure, recent analyses of present-day dynamic topography have tended to focus on instantaneous flow models (e.g., Conrad and Husson, 2009; Davies et al., 2019; Hager and O'Connell, 1979; Lithgow-Bertelloni and Silver, 1998; Ricard et al., 1993; Richards and Hager, 1984; Richards et al., 2020b; Steinberger, 2007, 2016).

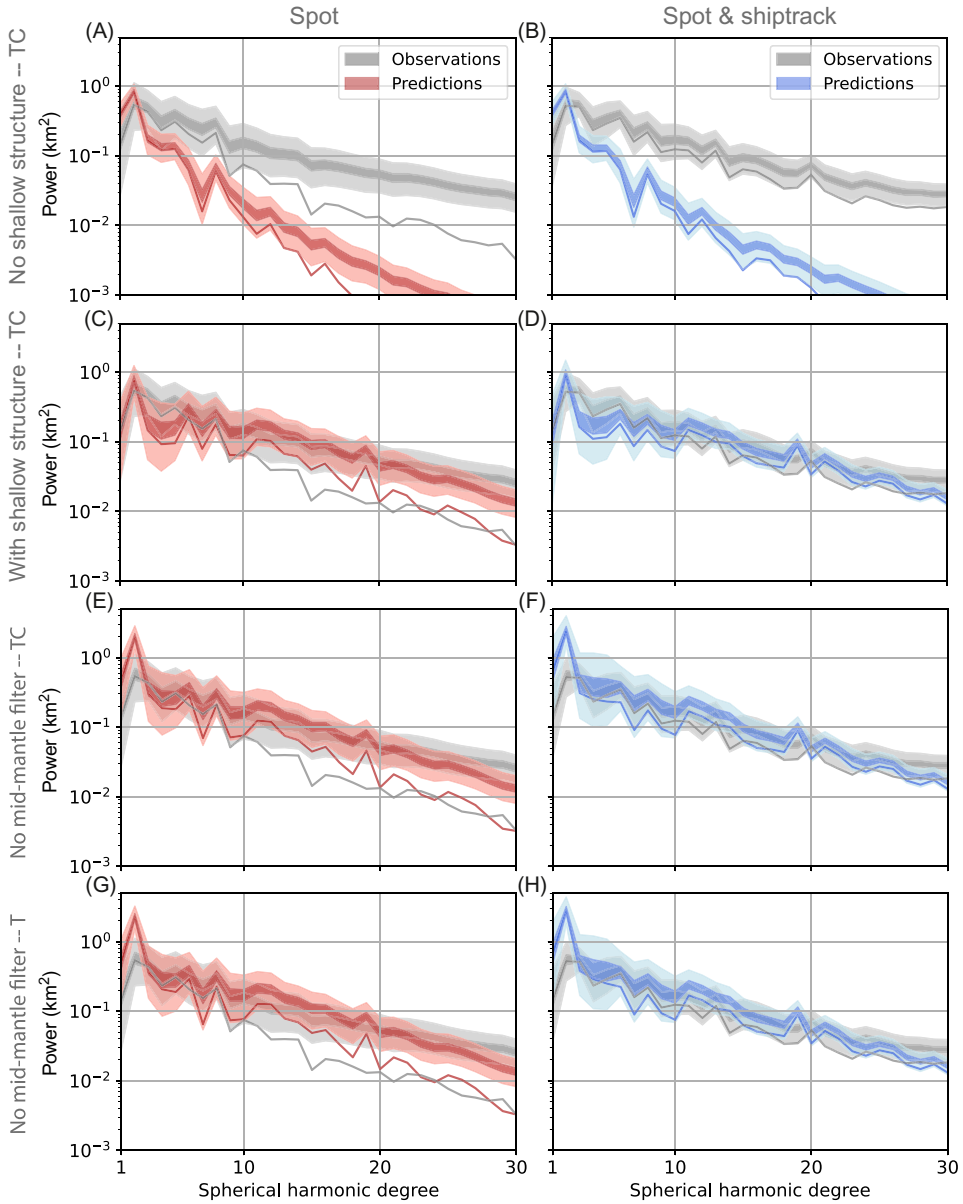

FIG. 2 Comparisons of water-loaded power spectra for inferred residual topography with synthetic predictions of dynamic topography. In all panels, the spectrum obtained using the observational constraints is shown in *gray*, both for the spot measurements only (A, C, E, G) and for the combined dataset of spot and shiptrack measurements (B, D, F, H). *Solid lines* represent the mean spherical harmonic coefficients; *colored bands* represent the ranges spanned by the central 50% and 99% of spectra computed for 100,000 randomly generated models consistent with the data (i.e., samples from the posterior distribution). In each panel, these observational constraints are compared to a model prediction of dynamic topography. Panels (A) and (B) are from the model that neglects mantle structure shallower than 250 km depth, sampled at either only spot or combined spot and shiptrack locations, respectively. Panels (C) and (D) are the same for the simulation that includes shallow structure: The observational data are more compatible with our simulation that includes shallow mantle structure. In panels (E and F), we show results from a model, where no filtering of degree-2 density anomalies has been performed in the mid-mantle (1000–2000 km depth range) and in panels (G and H) seismic structure is converted into physical structure assuming a pyrolite composition, with no chemically anomalous material at the base of LLVPs (purely thermal [T], as opposed to thermochemical [TC]). In both latter cases, power is dramatically over-predicted at long wavelengths.

In these calculations, flow velocities and pressures are calculated in relation to prescribed density and viscosity fields, using either a semi-analytical approach (e.g., Richards and Hager, 1984) or discretized numerical approaches (e.g., Davies et al., 2019).

2.4.1 Modeling approach and end-member cases

Assuming incompressibility and the Boussinesq approximation, the governing equations for instantaneous mantle flow are the Stokes and continuity equations, expressed in nondimensional form as:

$$\nabla \cdot \left[\mu\left(\nabla\vec{u} + \left(\nabla\vec{u}\right)^{T}\right)\right] - \nabla p = g\ \delta\rho\ \hat{k} \qquad (9)$$

$$\nabla \cdot \vec{u} = 0 \qquad (10)$$

where $\vec{u}$ is the velocity, p is the pressure, μ is the viscosity, ρ is the density, g is the gravitational acceleration, and $\hat{k}$ is the unit vector in the direction opposite to gravity. These equations describe the balance between driving (buoyancy) and resisting (viscous) forces at any instant in time and include no time dependence. For this reason, models that only incorporate Eqs. (9), (10) are termed as *instantaneous*: the velocity and pressure fields are computed for a prescribed density and viscosity structure. Dynamic topography can subsequently be computed from predicted radial stresses, τ_{rr}, at the surface via $h = \tau_{rr}/(\delta\rho_{\text{ext}} \cdot g)$, where $\delta\rho_{\text{ext}}$ is the density contrast between uppermost mantle density and air (continents: 3300 kg m^{-3}) or water (oceans: 2300 kg m^{-3}).

In the results that follow, we solve these governing equations inside a spherical shell, using a modified version of the Fluidity computational modeling framework (e.g., Davies et al., 2011, 2016; Kramer et al., 2012), recently validated against an extensive set of analytical solutions introduced by Kramer et al. (2021) and further benchmarked against published results from alternative spherical-shell mantle convection codes (e.g., Davies et al., 2013; Tackley, 2008; Zhong et al., 2008). In our simulations, the inner radius corresponds to the core-mantle-boundary (CMB) and the outer radius to Earth's surface, with free-slip mechanical boundary conditions specified at both boundaries. Models employ a fixed icosahedral mesh with a lateral resolution of ~50 km at the surface. This mesh is extruded in the radial direction, with radial spacing increasing linearly from 10 km at the surface to 100 km at the CMB.

We focus on two end-member simulations of global mantle flow. In the first, lateral variations in density and viscosity are ignored above 250 km depth, allowing us to quantify the first-order topographic expression of deeper mantle flow. In the second, we account for the effects of shallow mantle flow and its interaction with the lithosphere by incorporating variations in density and viscosity for the entire convecting mantle and lithosphere. In both cases, when converting normal stresses to dynamic topography, we assume a global water load at the surface. These simulations are similar to those of Davies et al. (2019), albeit with some important updates: (i) our tomographically derived density field has been modified to exploit a robust thermodynamic approach for converting between seismic and physical structure; and (ii) our radial viscosity profile has also been updated for consistency with the aforementioned conversion and to ensure that our model predictions are compatible with observations of Earth's geoid (discussed further below).

2.4.2 Physical properties: Density and viscosity

To determine the present-day mantle density field, we adopt the hybrid approach described in detail in Richards et al. (2022). Above 300 km depth, density is computed using the thermomechanically self-consistent parameterization described in Richards et al. (2020b), in which a series of independent constraints on upper-mantle temperature, seismic attenuation, and viscosity are used to calibrate an experimentally

derived parameterization of anelasticity for a particular seismic tomographic model (Yamauchi and Takei, 2016). In this case, we use the upper-mantle V_{SV} model of SL2013sv (Schaeffer and Lebedev, 2013), augmented with regional higher resolution V_{SV} models that employ the same tomographic procedure: SL2013NA for North America (Schaeffer and Lebedev, 2014); AF2019 for Africa (Celli et al., 2020a); and SA2019 for South America and the South Atlantic Ocean (Celli et al., 2020b), as outlined in Hoggard et al. (2020). Importantly, density variations related to the cooling of oceanic lithosphere are removed. This process involves subdividing the principal oceanic basins into 2 Myr bins, extracting density profiles from each location within a given bin, and stacking them to yield globally averaged age- and depth-dependent density changes. The difference between these mean values and those of the preliminary reference Earth model (PREM; Dziewonski and Anderson, 1981) is subtracted from the oceanic density field according to the local lithospheric age, ensuring that computed topography does not incorporate isostatic seafloor subsidence.

Below 400 km depth, the paucity of independent constraints on the covariation of V_S, temperature, attenuation, and viscosity forces us to adopt an alternative methodology. Over this depth range, we use Perple_X (Connolly, 2005, 2009) alongside the thermodynamic database of Stixrude and Lithgow-Bertelloni (2011) to determine equilibrium phase assemblages throughout the mantle as a function of composition, temperature and pressure, and their associated anharmonic V_S and density values. Temperature-dependent discontinuities in these properties that are caused by phase transitions are smoothed, since the anomalies they generate are too short wavelength to be captured by most seismic tomographic models. In addition, to account for anelasticity, anharmonic V_S is corrected using the approach of Matas and Bukowinski (2007), as outlined in the supplement of Richards et al. (2022). This procedure involves generating an ensemble of seismic quality factor (Q) profiles from the full range of possible upper and lower mantle anelastic parameters (e.g., activation energies, activation volumes, and frequency-dependence factors), discarding those that fall outside of independently constrained bounds, and then selecting the profile and associated parameters that produce the median value of average lower mantle Q. The pressure- and temperature-dependent V_S reduction associated with these values is then subtracted from the Perple_X-derived anharmonic V_S predictions. Having made these adjustments, tomographically inferred V_S can be converted to temperature and corresponding density for a prescribed mantle composition. Given their ability to simultaneously satisfy a range of geodynamic, geodetic, and seismological constraints, we adopt the TX2011 seismic tomographic model (Grand, 2002) and the compositional model of Richards et al. (2022), in which the mantle is assumed to be pyrolitic (Workman and Hart, 2005), aside from a ~200 km thick basal layer within large low velocity provinces (LLVPs) comprising a mechanical mixture of iron-enriched Hadean basalt (Tolstikhin and Hofmann, 2005) and pyrolite (~50% basalt; ~50% pyrolite). LLVPs are delineated using the $\delta V_S = 0.65\%$ velocity anomaly contour.

Between 300 and 400 km depth, where the sensitivity of the surface wave-dominated upper mantle model tends to zero, density anomalies are calculated using both methodologies independently. We then take their depth-weighted average in order to ensure a smooth transition in between the two parameterizations. The resulting models differ from those of Richards et al. (2022) only within the 1000–2000 km depth range, where instead of zeroing out buoyancy anomalies to combat inferred tomographic smoothing artifacts (Davaille and Romanowicz, 2020), a smooth high-pass filter of the form,

$$f(l) = -\left(\frac{l - l_{\min}}{l_{\max} - l_{\min}}\right)^4 + 2\left(\frac{l - l_{\min}}{l_{\max} - l_{\min}}\right)^2 \tag{11}$$

is convolved with the spherical harmonic coefficients of the density field, assuming a minimum degree, $l_{\min} = 1$, and a maximum degree, $l_{\max} = 8$. This procedure allows reliably imaged smaller-scale features to be retained, such as slabs and larger mantle plumes, while the long-wavelength, low-velocity "halo" above LLVPs is muted. As in Richards et al. (2022), we find that these adjustments are required for our models to generate predicted $l = 2$ geoid and dynamic topography amplitudes that are in reasonable agreement with the observed ratios, but also incorporate realistic convective structures from the mid-mantle.

An estimate of mantle temperature is also derived from tomography using the aforementioned approach. In contrast to the density field, however, age-dependent oceanic cooling trends are now retained. This temperature field controls the viscosity distribution in our models, which varies with depth and temperature, following the relation

$$\mu_r \cdot \exp\left[E_a(0.5 - T^*)\right] \tag{12}$$

Here, T^* is the nondimensional temperature, $E_a = 13.81$ controls the sensitivity of viscosity to this temperature, while μ_r varies with depth. The latter is set to ensure a mean radial viscosity profile that closely matches that of the purely depth-dependent model S10 from Steinberger et al. (2010), which has been constructed to be compatible with observations of Earth's geoid, heat flux, glacial isostatic adjustment, and CMB ellipticity. The resulting density and viscosity profiles are displayed in Fig. 3. Relative to S10, our mean viscosity profile incorporates a lower viscosity asthenosphere between 100 and 410 km depth, marginally higher viscosities between 660 and 1000 km depth, and a more muted reduction in viscosity below 2500 km depth toward the CMB.

2.4.3 Synthetic predictions of dynamic topography

Predicted dynamic topography from these simulations is shown in Fig. 4. The model without shallow structure (Fig. 4C) shares many characteristics with published models (e.g., Conrad and Husson, 2009; Flament, 2019; Flament et al., 2013; Rubey et al., 2017; Spasojevic and Gurnis, 2012; Steinberger, 2007), displaying long-wavelength topographic highs within the Pacific Ocean, southern and eastern Africa, and the North Atlantic Ocean, with lows extending across Central and South America, Europe, northern Africa, and southeast Asia. The simulation that also incorporates shallow structure (Fig. 4E), on the other hand, exhibits shorter wavelength features. Nonetheless, the Pacific domain is generally associated with a topographic high, albeit with a broad low off the west coast of South America and more localized lows in the northeast Pacific Ocean. Large topographic highs are visible in the western United States, the margins of Antarctica, southern and eastern Africa and adjacent to Iceland, with major lows focused along the AAD, the South Atlantic, the northwest Atlantic basin, and southeast Asia. These predictions closely resemble those of Steinberger (2016), Davies et al. (2019), and Richards et al. (2020b), who also incorporate shallow mantle and lithospheric structure, albeit with some spatial variability.

Following Davies et al. (2019), these predictive models are next sampled at the locations of spot and shiptrack oceanic residual topography estimates, thus enabling fully consistent comparisons with the observational constraints. The Gaussian process approach is subsequently used to perform an independent inversion for each model. The resulting power spectra are displayed in Fig. 2. For the model that neglects shallow structure (Fig. 2A and B), spectral power displays a clear peak at $l = 2$ and rapid drop off at higher l. This is inconsistent with the observational constraints, which show significant

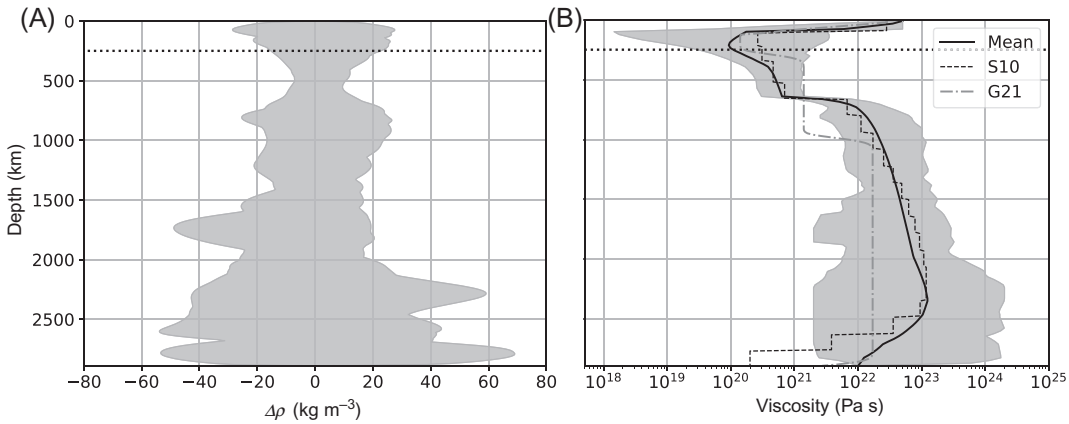

FIG. 3 Density and viscosity structure for mantle flow models. Panel (A) shows the range of density anomalies as a function of depth, and panel (B) shows the range of viscosities, in addition to the mean, at each depth. The purely depth-dependent model S10 from Steinberger et al. (2010) is displayed for comparison, alongside the profile of Ghelichkhan et al. (2021), G21, used for simulations presented in Section 3.3. In our simulation that neglects shallow structure, density, and viscosity variations above 250 km depth are omitted (above *horizontal dotted line*).

power at shorter wavelengths. For the model that incorporates shallow structure, spectral power also peaks at $l = 2$ (Fig. 2C and D), but it does not drop off as strongly at higher l. We note that the mean model predicts marginally more power ($\sim$0.75 km^2) than the observational constraints ($\sim$0.54 km^2) at $l = 2$, but, in general character, the spectrum is consistent with the observational constraints, with the range of plausible models overlapping at all l. This result represents an improvement on the fit between model prediction and observational data when compared to Davies et al. (2019), who, despite reproducing the general characteristics of the observational spectrum, generally over-predicted power across all spherical harmonic degrees. This improvement is principally driven by our revised approach for converting between seismic and physical structure in both the upper (Richards et al., 2020b) and lower (Richards et al., 2022) mantle.

2.4.4 Comparisons with the observed geoid

The shape of Earth's geoid, an equipotential surface of the gravity field that has been well constrained for decades through satellite geodesy (e.g., Kaula, 1967), depends not only on internal density anomalies, but also the boundary deflections that they produce at Earth's surface and CMB (e.g., Hager, 1984; Hager et al., 1985). Model predictions that satisfy observational constraints on dynamic topography must therefore also be compatible with the observed geoid (e.g., Flament, 2019; Ricard et al., 1993; Richards et al., 2022). To facilitate such a comparison, we have computed the synthetic non-hydrostatic geoid for our simulations using an analytical solution to the Poisson equation in spherical coordinates. In addition to the direct gravitational contribution of mantle density anomalies, contributions from dynamically induced boundary undulations (i.e., surface and CMB dynamic topography) are superimposed (e.g., Zhong et al., 2008). While our modeling approach allows us to capture the effects of lateral viscosity variations, we note that, in contrast to the previous geoid studies using the semianalytical propagator matrix technique (e.g., Ricard et al., 1993; Richards and Hager, 1984; Richards et al., 2022; Steinberger, 2016), our formulation does not account for self-gravitation.

Maps of the observed and predicted geoid, filtered up to spherical harmonic degree 50,

are presented in Fig. 4B, D, F, and H. The observed nonhydrostatic geoid height anomaly varies between − 121 and + 107 m, being dominated by highs in the African and Pacific regions that connect beneath South America, separated by a band of lows that run through Asia, the Indian Ocean, and the poles. These spatial patterns are generally well recovered by our model predictions: the model that neglects shallow structure yields a correlation coefficient (CC) of 56.1%, while the model that incorporates shallow structure yields a marginally improved correlation coefficient of 60.0%. It is clear from Fig. 4, however, that geoid amplitudes predicted by our synthetic models are slightly lower than the observations: for the model neglecting shallow structure, amplitudes range between −73 and +94 m, while they range between −89 and +93 m in the model incorporating shallow structure. This amplitude reduction is reflected in the geoid variance reduction (VR) diagnostics, which are ∼31.5% and ∼36.0%, respectively. We note that the similarity in predicted geoid anomalies for these synthetic models is expected given that it is dominated by long-wavelength structure in the deep mantle (e.g., Colli et al., 2016; Hager, 1984; Hager et al., 1985), which remains consistent between both simulations.

Our geoid VR diagnostics are lower than those of Steinberger (2016), who recorded values of ∼70% for many cases, and Richards et al. (2022), who recorded a value of ∼59% for the density model used herein. It should be noted, however, that these results are not directly comparable: as outlined earlier, the approach used herein allows us to resolve the effects of lateral viscosity variations but neglects self-gravitation, whereas the semianalytical approach utilized by Steinberger (2016) and Richards et al. (2022) neglects lateral viscosity variations but accounts for self-gravitation. Although we cannot directly quantify the effects of self-gravitation here, it is known to impact dynamic topography and the geoid at long wavelengths (e.g., Zhong et al., 2008). Its omission, therefore, likely explains part of the deterioration in geoid VR relative to the previous studies. On the other hand, we are able to explore the significance of lateral viscosity variations. To do so, we have examined a simulation where viscosity varies as a function of depth only, using the depth-averaged viscosity of our model with shallow structure (Fig. 3B). The geoid VR is improved by this test, driving our results closer to the previous studies. This interesting result does not imply that the mantle's viscosity varies with depth only: It is well known that lateral viscosity variations are fundamental in dictating the planform of mantle convection, being required to reproduce imaged slab morphologies (e.g., Garel et al., 2014; Goes et al., 2017) and key characteristics of mantle plumes (e.g., Davies, 1999; Griffiths and Campbell, 1991; Ito et al., 2003). Rather, since we have chosen to calibrate our simulations such that the depth-averaged viscosity closely matches the S10 radial profile from Steinberger et al. (2010), this result suggests that the future efforts to constrain mantle viscosity from observations including mantle heat flux, postglacial rebound, and CMB ellipticity should carefully consider the role of lateral viscosity variations, alongside self-gravitation, to determine how these factors combine to influence the predicted geoid.

The results presented here, alongside those in Section 2.4.3, demonstrate that models incorporating shallow mantle structure can simultaneously satisfy observational constraints on both residual topography and the geoid (noting the shortcomings outlined earlier), whereas the model that neglects shallow structure only provides a satisfactory fit to the latter. Taken together, these comparisons imply: (i) a dominant role for deep-mantle flow in dictating Earth's dynamic topography and geoid expression at long wavelength and (ii) an important role for shallow processes, involving the interaction between asthenospheric flow and lithospheric structure, in dictating the shorter-wavelength components of dynamic topography and the general character of the power spectrum.

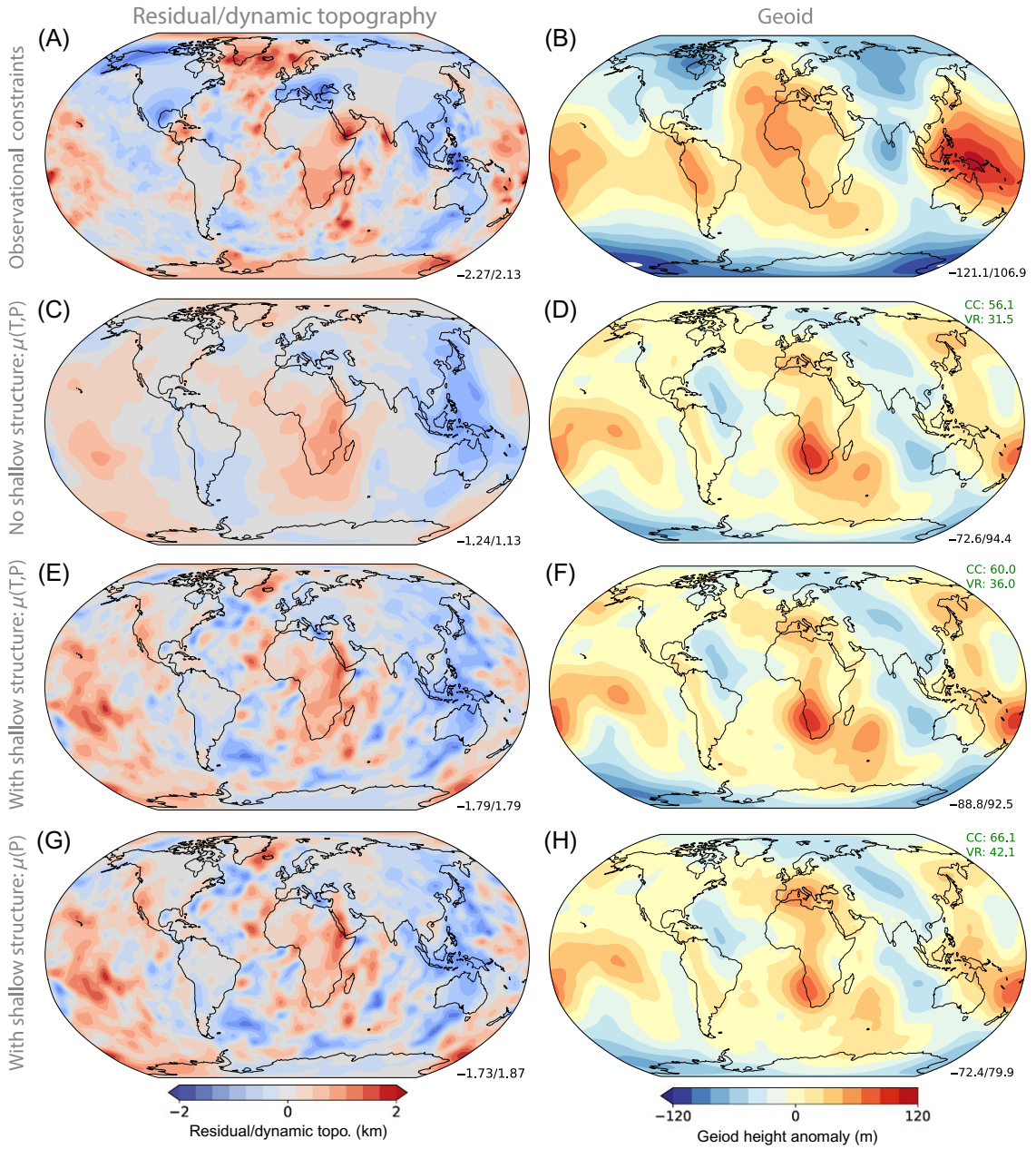

FIG. 4 Inferred water-loaded residual topography (A) and predicted dynamic topography (C, E, G), alongside observed (B) and predicted nonhydrostatic geoid height anomalies (D, F, H). The reference geoid height anomaly comes from Pail et al. (2010) corrected for hydrostatic effects as in Chambat et al. (2010). Panels (C, E, G) display predicted water-loaded dynamic topography from instantaneous flow models. In panel (C), density and viscosity heterogeneity is neglected at depths shallower than 250 km, whereas in panel (E) it is included. The model shown in panel (G) incorporates shallow density heterogeneity but includes a pressure-dependent viscosity only, corresponding to the depth average of the model shown in (E). Minimum and maximum values for each map are given in the lower-right corner. For geoid maps, the correlation coefficient (CC) and variance reduction (VR), both in %, between predicted and observed geoid is also shown in the upper-right corner (see Richards et al., 2022 for details of CC and VR calculations).

2.5 Summary of present-day dynamic topography

Observational estimates of dynamic topography, alongside measurements of the geoid, provide a fundamental constraint on the structure and dynamics of Earth's mantle. While the long-wavelength harmonics of the geoid have been well constrained for decades using satellite geodesy (e.g., Kaula, 1967), observational constraints on dynamic topography are still being developed. A recently compiled global database of residual topography measurements within the world's oceans provides the most robust constraint on present-day dynamic topography that is currently available (Hoggard et al., 2017). Nevertheless, these measurements are made at discrete, unevenly distributed locations on Earth's surface and, hence, it is challenging to make inferences concerning global properties.

Building on a series of studies (e.g., Davies et al., 2019; Hoggard et al., 2016, 2017; Steinberger, 2016; Steinberger et al., 2019; Yang and Gurnis, 2016; Yang et al., 2017), Valentine and Davies (2020) used a novel approach based upon the statistical theory of Gaussian processes (Valentine and Sambridge, 2020a, b) to infer the spatial pattern, wavelength, and amplitude of global residual topography. Results, which have been reviewed herein, indicate that the associated spherical harmonic power spectrum peaks at $l = 2$, with power likely in the range 0.47–0.70 km^2 for a global water load. This value decreases by over an order of magnitude at $l = 30$, with around 86% of the total power concentrated in degrees 1–3. Comparisons between this spectrum and updated synthetic predictions from instantaneous models of mantle flow demonstrate that the long-wavelength components of Earth's residual topography are principally driven by deep-mantle flow, but shallow processes involving the interaction between asthenospheric flow and lithospheric structure are also crucial in explaining the general form of the power spectrum. This relationship is to be expected based on the sensitivity kernels that illustrate how effective density anomalies at different depths and spherical harmonic degrees are at creating topography (e.g., Colli et al., 2016; Hager, 1984; Hager and Richards, 1989; Hoggard et al., 2016; Steinberger, 2016).

Although we are now at the stage where model predictions of dynamic topography and observational constraints on residual topography are broadly consistent with one another, until recently, this was not the case. This review demonstrates that reconciliation of model predictions and observational constraints, in a manner that is also compatible with the geoid, requires a carefully constructed dataset of residual topography (Hoggard et al., 2017), robust methods for inferring global characteristics from this data (Davies et al., 2019; Valentine and Davies, 2020), a carefully calibrated approach for converting from seismic velocities to physical structure (Richards et al., 2020b, 2022), and computational modeling tools that are capable of using the resulting mantle structure as input (Davies et al., 2019).

Some aspects, however, require further work. For example, at present, there is no modeling framework available for computing mantle flow, while simultaneously accounting for the effects of lateral variations in viscosity and the full (nonlinear) impact of self-gravitation. As demonstrated in Section 2.4, this shortcoming affects our ability to directly compare synthetic predictions with observations of Earth's geoid and the development of such a capability is an important avenue for future research. Furthermore, although the range of plausible models for our simulation incorporating shallow structure overlaps with the observational estimates of dynamic topography at all degrees, our flow models generally predict too much power at $l = 2$. This issue is consistent with the findings of Steinberger et al. (2019), although our amplitudes are only ~10% too large, rather than a factor of 2, as is visually demonstrated in Fig. 5, where we plot the $l =$ 1–3 components of both the residual topography

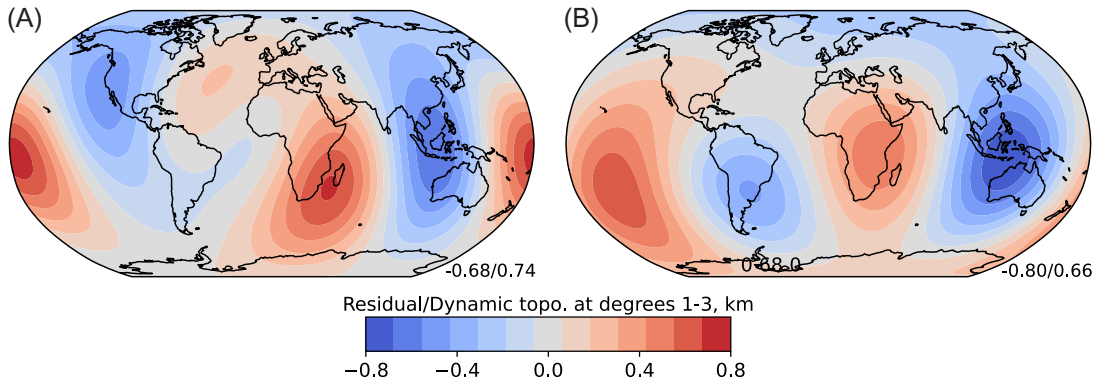

FIG. 5 Long-wavelength water-loaded residual topography for (A) the spot and shiptrack-derived observational constraints and (B) our predictive flow model incorporating shallow structure. Note that results have been filtered to include only spherical harmonic degrees 1–3.

measurements and our flow model predictions (sampled at spot and shiptrack locations and spectrally analyzed in a self-consistent manner). Although the peak amplitude of positive dynamic topography is in reasonable agreement between observations and predictions (a difference of only 0.08 km), the difference in peak negative values is larger, being −0.68 km for observations versus −0.80 km for predictions. Inspection of the spatial maps reveals that it is in the region of the southeast Asia subduction zones that predicted drawdown is currently too large.

Nevertheless, the principal reason for our improved ability to match long-wavelength dynamic topography is our filtering out of degree-2 density anomalies in the mid-mantle (1000–2000 km depth range). Richards et al. (2022) demonstrate that it is $l = 2$ structure at these depths that erroneously inflates dynamic topography amplitudes in mantle flow simulations, and also breaks the observed ratio between geoid and long-wavelength dynamic topography. This issue is further highlighted in Fig. 2E–H, where we plot predicted dynamic topography power spectra for simulations similar to the case with shallow structure examined herein, but with no filtering of degree-2 density anomalies in the mid-mantle. The first case assumes a thermochemical LLVP with a consistent composition to the cases examined thus far (Fig. 2E and F), while the second assumes a pyrolitic composition with density anomalies purely driven by temperature variations (Fig. 2G and H). In both scenarios, power is dramatically overpredicted at long wavelengths, particularly at $l = 2$. Given the long ray paths for body waves, low density of crossing rays, and broad sensitivity of normal modes to velocity structures at these depths, it is perhaps of no surprise that there appears to be substantial smearing of deep LLVP mantle structure upwards to shallower depths, and also a smoothing of higher frequency structure, such as plumes and slabs, into lower spherical harmonic degrees, as recently suggested by Davaille and Romanowicz (2020), and demonstrated in synthetic models using the S40RTS resolution operator of Ritsema et al. (2007, 2011) by Davies et al. (2012) and Jones et al. (2020). We acknowledge that our current approach to dealing with this problem is somewhat rudimentary and keenly await further tomographic studies that might investigate these potential resolution issues.

We emphasize that fine details of the predicted dynamic topography in our simulations and their associated power spectra are sensitive to several model parameters. These include: (i) the depth and lateral dependence of mantle viscosity, which remains poorly constrained (e.g., Ballmer et al., 2017; Lau et al., 2017; Marquardt and Miyagi, 2015; Rudolph et al., 2015) and may influence coupling between upper and lower mantle, the transmission of stress across the asthenosphere to the lithosphere, and through the lithosphere to the surface; (ii) the seismic tomography model used as a basis for defining the mantle's density and thermal structure — although tomographic models now show broad similarity in the distribution of heterogeneity at a large scale (Lekic et al., 2011), they differ in amplitude and in the distribution of smaller-scale heterogeneity; and (iii) the lack of phase transitions in our models, which will influence how density anomalies at various depths couple to the surface and CMB (e.g., Steinberger, 2007; Thoraval and Richards, 1997), impacting both dynamic topography and geoid predictions. Nonetheless, our models are based upon a reasonable set of parameters that allow us to illustrate the likely roles of shallow and deep-mantle flow in generating Earth's surface response. These insights gained from analysis of the present-day datasets are of fundamental importance if we are to accurately reconstruct the evolution of dynamic topography through the geological past.

3. Dynamic topography into the geological past

3.1 Observational constraints

Investigating the temporal evolution of dynamic topography requires identification and dating of geological features that can track changes in elevation through time. The accuracy of each individual constraint depends upon its indicative range of formation (i.e., the range of elevations that it could have formed at), and by far the most robust markers tend to be generated in the vicinity of sea level since, in this setting, a variety of starkly contrasting geological environments operate over a narrow paleo-elevation band. For example, many marine organisms only grow in the shallow waters of the photic zone, hence uplift and subsidence of features such as coral reefs can be used to place tight bounds on the amplitude and rates of evolving dynamic topography (e.g., Austermann et al., 2017; Czarnota et al., 2013; DiCaprio et al., 2010; Stephenson et al., 2019). Other proxies for former sea levels that have been used to reconstruct vertical motions include estuarine and deltaic sediments (e.g., lignites and coals), paleosols, fluvial base levels in the vicinity of coastlines, transitions between erosional and depositional environments within basin stratigraphy (including unconformities and the geometries of clinoform packages), and other uplifted marine rocks. Away from sea level, techniques involving paleoaltimetry (e.g., clumped-isotope analysis), biological tiering (e.g., leaf palynology), sedimentary deposits from ocean currents, and the carbonate compensation depth (CCD) have also been exploited, but suffer from larger uncertainties due to the wider indicative range associated with these paleo-elevation proxies. For an in-depth review of these approaches and many others, we refer the reader to the recent review paper of Hoggard et al. (2021).

While the most robust observational constraints on dynamic topography at the present day are obtained in the oceanic realm (Section 2), it remains a relatively poor place to attempt reconstruction of changes in dynamic topography through time for two important reasons. First, in spite of possible interactions with the CCD (e.g., Campbell et al., 2018), a transient, kilometer-scale uplift and subsidence event of 6-km-deep abyssal ocean floor is less likely to

have an impact on the geological record than if that cycle were to occur on a continental shelf and, therefore, cross the boundary between depositional and erosional settings (e.g., Hartley et al., 2011). Second, the geological record in the ocean basins extends to only ~200 Ma before subduction destroys it, whereas continental features such as cratonic basins can survive for billions of years and, therefore, potentially store signals associated with dynamic topography for much longer temporal durations (e.g., Crosby et al., 2010; Young et al., 2021). Thus, existing observational estimates for changes in dynamic topography are generally focused on continental interiors and their surrounding margins. It is not possible to cover all of these studies in sufficient detail here, so we instead restrict ourselves to summarizing those related to Cenozoic vertical motions in North America, Australia, and Africa in order to permit later comparison with numerical simulations of mantle flow in Section 3.3.

North America: The geological record of Mexico, the United States, and Canada contains substantial evidence for transient vertical motions throughout the Cenozoic Era. One of the most iconic examples of large-scale marine incursions comes from the western United States, where a phase of Cretaceous drawdown lead to the development of an interior seaway that was up to ~1400 km wide and resulted in more than 3 km of sedimentary deposition in its deeper western portions (e.g., Bond, 1978b; Sloss, 1963). There is a general absence of large-scale tectonic features in the Upper Cretaceous stratigraphy that might indicate a flexural or extensional basin formation mechanism (e.g., thrust or normal faults, horsts, and grabens). Combined with the timing and widespread nature of the depocenter, this observation lead several early studies to link formation of the seaway to underlying mantle flow, in particular subsidence above the downgoing Farallon slab (e.g., Bond, 1978b; Burgess et al., 1997; Cross and Pilger, 1978; Mitrovica et al., 1989). The fact that this marine stratigraphy is now exposed at elevations of up to ~2 km above sea level attests to subsequent dynamic rebound of the seaway following westward passage of the region over the downgoing slab. Several studies have focused on reconstructing the rates and timing of this uplift (see Fernandes et al., 2019 for a comprehensive review). Evidence that has been exploited includes the age and elevation of uplifted marine and coastal rocks, paleoaltimetry estimates from clumped-isotope analysis, the incision and retreat of river profiles draining the region, estimates of sedimentary flux into surrounding basins, and landscape denudation measurements made from techniques including apatite (U–Th)/He and fission track analysis (e.g., Flowers et al., 2007; Huntington et al., 2010; Roberts et al., 2012b; Robinson Roberts and Kirschbaum, 1995; Stephenson et al., 2014; Winn et al., 2017). While the total amplitude of cumulative uplift is well constrained, there has been considerable debate concerning its timing. Some studies suggest that most of the present-day topography had already formed by Eocene times, while many others argue for multiple stages of uplift, including a substantial phase of Late Neogene growth that continues today. This latter phase coincides with extensive intraplate volcanism throughout the Colorado Plateau and Wyoming, and has been linked to incursion of warm asthenospheric material (as manifest by slow subplate seismic velocities) and arrival of the Yellowstone plume (Klöcking et al., 2018). Elsewhere in North America, there have been arguments for similar Cenozoic uplift (or incision) events throughout central Mexico, the Appalachian mountains, the Rockies, and in parts of the Canadian shield (e.g., Ault et al., 2013; Chamberlain et al., 2012; McKeon et al., 2014; Rovere et al., 2015; Stephenson et al., 2014). By contrast, further to the east on the Atlantic passive margin, an anomalously thick sequence of shallow-water sediments appears to indicate a widespread phase of Neogene subsidence (e.g., Cloetingh

et al., 1990; Steckler and Watts, 1978). Recent stratigraphic analyses estimate that 0.3–1.0 km of water-loaded drawdown has occurred over the last 20 Myr, centered on the Baltimore Canyon Trough (Morris et al., 2020). Since the rifting event responsible for forming the passive margin ended in the Early Jurassic times and there is no evidence of extensional tectonics in any of the Neogene stratigraphy, a phase of dynamic drawdown appears to be the most likely driving mechanism (Kominz et al., 2016; Morris et al., 2020).

Australia. Analogous to the situation in North America, much of the central and eastern portions of present-day Australia were flooded by an inland sea in mid-Cretaceous times (Frakes et al., 1987). Today, this marine stratigraphy is exposed onshore (primarily within the Eromanga Basin), and this transient subsidence-rebound event has been linked to a similar story of a downwelling slab in the upper mantle (Gurnis et al., 1998). On a broad scale, Neogene vertical motions in Australia have been dominated by uplift in the south and subsidence in the north. Geological evidence for this behavior includes the relative width of continental shelves (narrow in the south, wide in the north), the stratigraphic architecture of Neogene sediments (offlap in the south, onlap in the north), and a series of paleoshorelines that are uplifted and exposed onshore in the south, but drowned in the north (Sandiford, 2007). Stratigraphic analysis and backstripping of carbonate clinoforms from the Northwest Shelf indicate that a water-loaded subsidence event of up to 600 m has occurred since ~10 Ma (Czarnota et al., 2013). The general picture of down-to-the-north Cenozoic tilting is, however, punctuated by some shorter wavelength uplift and subsidence events within the continent. In particular, there are several lines of evidence pointing to localized uplift of the Eastern Highlands by up to 2 km sometime since Jurassic/Cretaceous times, although there remains significant controversy over the age and rates of this vertical motion (e.g., Bishop, 1988; Holdgate et al., 2008; Jones and Veevers, 1982). Nevertheless, multiple different datasets including uplifted marine rocks, speleothem records, palynology, river profile modeling, sedimentary flux into fringing basins, and the age and morphology of basaltic volcanism indicate significant Cenozoic uplift of the margin that likely continued into Neogene times (Ball et al., 2021; Czarnota et al., 2014; Engel et al., 2020; Fernandes and Roberts, 2021; Holdgate et al., 2008; Wellman, 1987).

Africa. It has been known since the earliest continental-scale studies of marine incursion that Africa has undergone several cycles of epeirogenic motions during Cretaceous and Cenozoic times (Bond, 1978a, 1979; Sahagian, 1988). Today, African topography is dominated by a large, high-elevation plateau in the south that steadily dies away northwards, while the entire continent is punctuated by a series of shorter wavelength domes and intermediate basins that have been termed "basin-and-swell" morphology (Burke et al., 2008). Once again, the timing and rates of uplift are heavily debated, but the classical view that much of the topography had existed since passive margin formation in the Jurassic and Early Cretaceous periods is now understood to be largely incorrect. Uplifted marine and coastal rocks dating from the Late Cretaceous through to the Eocene can be found at the present-day elevations of more than 500 m in parts of north and east Africa (Bond, 1978a; Fernandes and Roberts, 2021; Sahagian, 1988). Several prominent planation surfaces, often exhibiting well-developed chemical weathering profiles and sometimes blanketed in younger sedimentary and volcanic rocks, have been dated and mapped throughout the continent and attest to a multistage uplift history since 40 Ma (e.g., Baby et al., 2018; Chardon et al., 2016; Friedrich et al., 2018; Guillocheau et al., 2018; Sembroni et al., 2016). The erosion and supply of clastic material to surrounding

continental margins exhibits a similarly pulsed history — for example, two prominent phases of erosion appear to have occurred in the Zambezi catchment from 34 to 24 Ma and 10 Ma to recent (Walford et al., 2005). Further south, the Limpopo delta shows an increase in clastic flux from 23 Ma onwards that is likely due to Miocene uplift of the northeastern part of the South African Plateau (Said et al., 2015). Further evidence for Cenozoic unroofing of parts of the continental interior comes from thermochronological studies of denudation. For example, (U–Th)/He thermochronology on granitic basement rocks and kimberlites across southern Africa indicates that the plateau planation surface likely formed in response to mid-to-late Cretaceous incision events that propagated from west to east across the continent, but generally limit Cenozoic unroofing to less than 1 km (Flowers and Schoene, 2010; Stanley et al., 2015). Nevertheless, there are several additional strands of evidence pointing to substantial Neogene uplift, including a large angular unconformity on the Angolan continental shelf (Al-Hajri et al., 2009), quaternary marine terraces that have been uplifted in Kenya, Angola, and Madagascar (Guiraud et al., 2010; Odada, 1996; Stephenson et al., 2019), and uplift histories determined from inversion of longitudinal river profiles (O'Malley et al., 2021; Paul et al., 2014; Roberts and White, 2010; Roberts et al., 2012a; Wilson et al., 2014). Interregional Cenozoic hiatus surfaces exhibit a strong expansion of total unconformable area for the base of Miocene outcrops, suggesting that the preceding period likely involved substantial uplift across much of southern Africa (Carena et al., 2019; Hayek et al., 2020). There was also a Neogene flare up in intraplate volcanism at many of the topographic swells across northern Africa (Ball et al., 2019). Taken together, the Cenozoic history of epeirogeny in Africa appears to involve a long wavelength, potentially early uplift of much of southern Africa, which is punctuated by renewed uplift and sporadic volcanism of several shorter wavelength domes throughout the African and Arabian continents in Neogene times.

3.2 Computational approaches for dynamic topography reconstructions

As is evident from the instantaneous flow models presented in Section 2.4, our ability to predict dynamic topography into the geological past requires knowledge of the thermochemical state of the mantle at previous points in Earth's history. Direct seismological and geodetic constraints on mantle structure, however, are limited to the present day, which represents a major obstacle for time-dependent computational models that aim to reconstruct the evolution of dynamic topography in space and time.

As explained earlier, the coupled Stokes and continuity equations (9) and (10) are instantaneous. For time-dependent simulations of mantle dynamics, these equations should be augmented with additional conservation laws describing the temporal evolution of mantle heterogeneity. These laws appear in the form of energy and, in the case of flow with multiple chemical compositions, compositional equations. Assuming isochemical flow, the energy equation, expressed once again in its nondimensional form under the Boussinesq approximation, is:

$$\frac{\partial T}{\partial t} + \boldsymbol{u} \cdot \nabla T = \kappa \Delta T + \phi \tag{13}$$

where T is temperature, t is time, κ is thermal diffusivity, and ϕ is a heat source term. Eq. (13) is coupled to the Stokes equation through an equation of state that relates density variations to temperature. Eqs. (9), (10), and (13) can be solved for velocity, pressure, and temperature, given appropriate boundary conditions at the surface and CMB, and an initial condition for the mantle's thermochemical structure. The

latter is of fundamental importance given that the spatial and temporal evolution of mantle convection is uniquely determined by its initial condition. The lack of direct constraints on mantle structure in the past — specifically, this unknown initial condition — is the main difficulty of inferring mantle flow and associated dynamic topography into the past. As illustrated in the schematic of Fig. 6A, the strong sensitivity of the mantle's evolutionary pathway to this initial condition means that without knowing it, we cannot accurately reconstruct the mantle's evolution from *forward models*, even for the most recent Mesozoic and Cenozoic history of our planet (e.g., Bunge et al., 2003).

The initial condition problem can be at least partially overcome through data assimilation (e.g., Bunge et al., 2002; Hager and O'Connell, 1979). As stated by Bunge et al. (2003), simply put, the purpose of data assimilation in a mantle convection model is to use all available information to determine, as accurately as possible, the state of mantle flow. From an algorithmic point of view, data assimilation is often implemented through sequential filtering (e.g., Wunsch, 1996): here, the model is run forward in time and, whenever an instant is reached where observations are available, the model is "updated" or "corrected." The amplitude of the correction can be determined in an optimal sense using schemes such as the Kalman filter (e.g., Bocher et al., 2018; Wunsch, 1996), with the model subsequently restarted from the updated state, and the process repeated until all available information has been assimilated.

Mantle circulation models, where plate tectonic reconstructions are integrated chronologically, provide an end-member class of data assimilation approach. In these models, reconstructed plate velocities (e.g., Müller et al., 2016b; Seton et al., 2012; Stampfli and Borel, 2004), often processed via the open-source GPlates software (e.g., Gurnis et al., 2012; Müller et al., 2018b), are either prescribed through a kinematic boundary condition (e.g., Bunge et al., 1998, 2002; Davies et al., 2012; Rubey et al., 2017), or through an approach that tries to better capture the expected thermal structure, thickness, dip angle, and upper mantle descent rate of slabs (e.g., Bower et al., 2015; Flament, 2019; Flament et al., 2017; Hassan et al., 2016). In both scenarios, it is assumed that the imposed tectonic reconstructions are error free, which is a major shortcoming given that uncertainties in these reconstructions are substantial and increase further into the geological past. A second drawback of this approach is that the imposed plate velocities may be inconsistent with the underlying force balance (e.g., Bocher et al., 2016; Forte and Peltier, 1991; Glišović et al., 2012; Han and Gurnis, 1999; Lowman, 2011). Nonetheless, the approach has been demonstrated to facilitate forward modeling simulations, where the predicted distribution of the present-day heterogeneity closely mimics that of Earth's mantle, as imaged through seismic tomography (e.g., Barry et al., 2017; Bunge et al., 2002; Davies et al., 2012; Flament, 2019; Flament et al., 2017; McNamara and Zhong, 2005; Schuberth et al., 2009), highlighting the central role of plate tectonics in organizing underlying mantle flow. As will be discussed further in Section 3.3, when the surface deflections from these simulations are examined through time, they are able to reproduce many of the long-wavelength observational constraints on dynamic topography through the Cenozoic Era, although shorter-wavelength variations are not captured. The consistency with observational constraints also deteriorates further back in time (e.g., Flament et al., 2013; Müller et al., 2018a; Rubey et al., 2017), due to the impact of the prescribed (arbitrary) initial condition, although the recent work to extend plate tectonic reconstructions further into the geological past (e.g., Merdith et al., 2021; Young et al., 2019) offers a potential avenue for reducing the dependence on the unknown initial condition (e.g., Cao et al., 2021; Colli et al., 2015; Davies et al., 2012; Flament, 2019; Zhang et al., 2010).

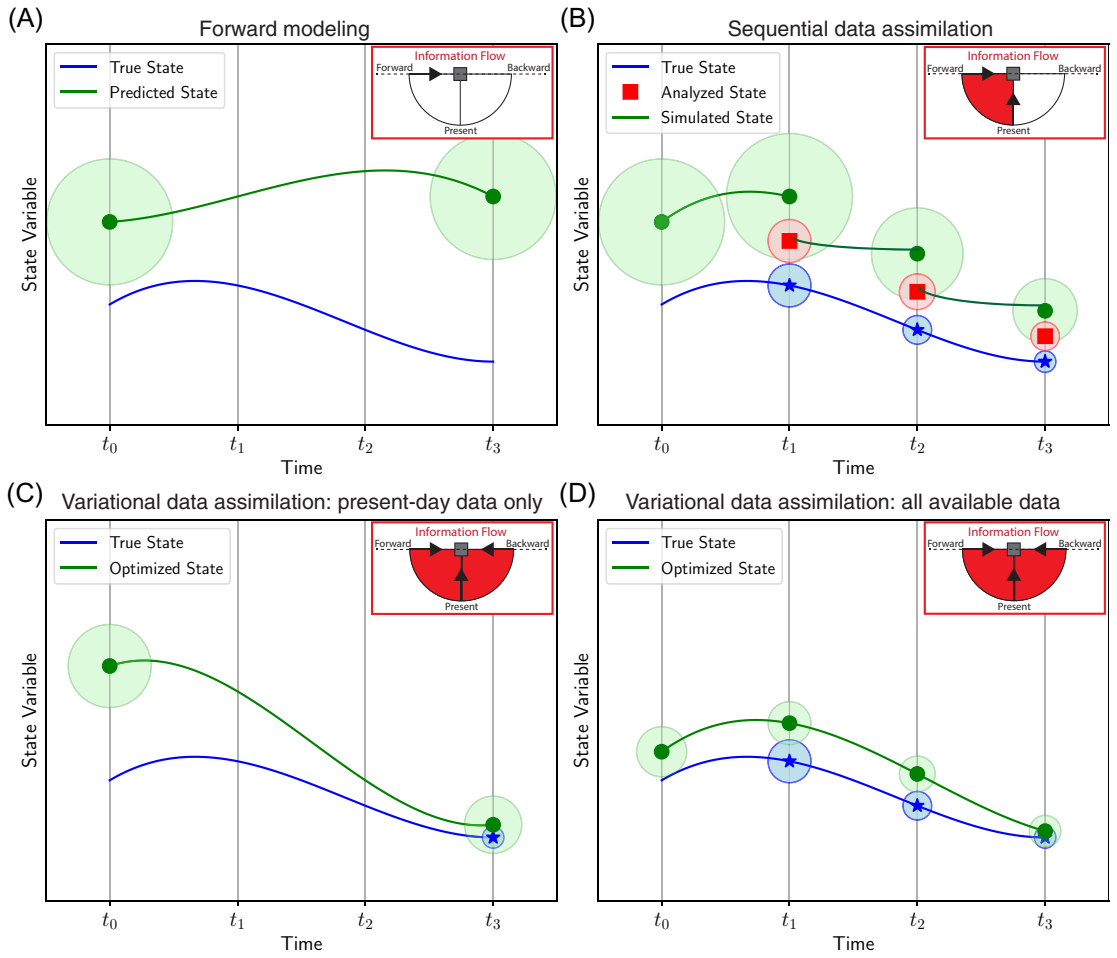

FIG. 6 Illustration of different procedures available for estimating mantle structure into the geological past: (A) forward modeling prediction, where an unknown initial condition is estimated at t_0, with prediction error, measured as the distance between the predicted and true state, growing in time; (B) sequential data assimilation — having estimated an initial condition at t_0, the forward model is run until t_1. An analysis is subsequently undertaken from the resulting prediction and the available observation, and a new prediction computed until the next observation at t_2. The process is repeated until t_3. The information flow diagram depicts how information is carried from both the past and present, using current data; (C, D) variational data assimilation, via an adjoint model, capable of carrying information explicitly backward in time. In (C), observational data that constrain present-day mantle structure (e.g., images from seismic tomography) are used to optimize the unknown initial condition: with limited data, the predicted initial condition has large uncertainty. This can be reduced, and the evolutionary pathway more tightly constrained, if data from different points in space and time can be brought to bear on the problem, as illustrated in (D). Here, all available observations between t_3 and t_0 contribute to the analysis. We note that, in reality, this data is scattered in space and time. The true (unknown) signal is represented by the *solid blue line*. Observations (*blue stars*), predictions (*green circles*), and analyses (*red squares*) are surrounded by ellipsoids of a size proportional to the estimated uncertainty. *Modified from Carrassi, A., Bocquet, M., Bertino, L., Evensen, G., 2018. Data assimilation in the geosciences: an overview on methods, issues, and perspectives. WIREs Clim. Change 9, e535.*

To circumvent the key shortcomings of mantle circulations models, Bocher et al. (2016) developed a novel *sequential data assimilation* approach, based upon a suboptimal Kalman filter, which integrates a time series of surface observations chronologically into a mantle convection model until all observations are taken into account. Whenever an observation is available, the analysis evaluates the most likely state of the mantle at this time, considering a prior guess. By running multiple simulations simultaneously to produce multiple evolutionary states, this approach is able to account for observational uncertainties, including those in plate tectonic reconstructions, while also allowing surface velocities to evolve more consistently with the underlying force balance. In contrast to the mantle circulation approach described earlier, surface velocities are only assimilated at specific points in time, and these observational constraints are weighted with those of the convection simulations at that time, rather than being fully prescribed. The approach of Bocher et al. (2016) was extended by Bocher et al. (2018) using a more advanced sequential data assimilation method, built around an ensemble Kalman filter (EnKF) (e.g., Burgers et al., 1998; Evensen, 1994). At each point in time, the EnKF approximates the probability density function of the state of the system, via a finite ensemble of states. As noted by Bocher et al. (2018), this method is able to exploit information across the ensemble more accurately and, accordingly, is able to provide a more formal estimate of uncertainty. This avenue of research is highly promising and will likely open up new opportunities for geodynamical research, particularly in the context of improving our treatment of uncertainties in plate tectonic reconstructions. To date, however, due to the computational cost of performing numerous global three-dimensional (3D) spherical simulations, the approach has not been applied to 3D spherical simulations exploiting real-Earth data at realistic convective vigor, which is of fundamental importance when reconstructing the spatial and temporal evolution of mantle flow and its impact at Earth's surface (e.g., Davies and Davies, 2009; Nerlich et al., 2016).

An appealing aspect of sequential filtering and the approach advocated by Bocher et al. (2016, 2018) is that updates are continuously applied to the convection model, with each new observation used to correct the latest model state and, as a result, the consistency between model predictions and observations tends to improve toward the present day as more and more observations are assimilated. There is, however, a fundamental drawback: because of the sequential nature of the assimilation, each observation is used only once and influences the model only at later times. As illustrated in Fig. 6B, information propagates from the past to the future, but not back into the past. This limitation is a major disadvantage in mantle convection studies, where our knowledge of the mantle at the present day is more detailed than at any earlier time. It is therefore necessary to explore a formulation capable of carrying information explicitly backward in time or, more precisely, one that allows estimation of a time-dependent model of mantle evolution that best fits all available constraints. We term this process *inverse geodynamics*, where the present-day and time-dependent observations are propagated backwards through geological history.

The main challenge in backward-in-time propagation of information is the unconditional instability of diffusive processes when one reverses time stepping. The most computationally straightforward approach for addressing this issue comes from the so-called *backward advection* method. Here, backward-in-time modeling of mantle flow is achieved by reversing the direction of gravity in the Stokes equation, with thermal diffusion either ignored or set to a small value. While the latter ensures numerical stability, it causes diffusion to act in the wrong direction during backwards-in-time integration. Using the present-day mantle

heterogeneity, as inferred from seismic observations, Steinberger and O'Connell (1998) simulated mantle flow backwards in time from the present day to examine the advection of plumes. A similar approach was used by Conrad and Gurnis (2003) to examine uplift of the African continent over the Cenozoic Era and Moucha et al. (2008) to investigate the stability of continental platforms. Ignoring thermal diffusion, of course, leads to unrealistic dynamics in regions of the mantle dominated by diffusion, such as the thermal boundary layers at Earth's surface and CMB. Given that the analyses of the present-day dynamic topography presented in Section 2.4 demonstrate a strong sensitivity to shallow mantle structure and flow, the backward advection approach is therefore of limited use in reconstructing the evolution of dynamic topography into the geological past.

The shortcomings of backward advection can be partially overcome using the quasi-reversibility (QRV) method, originally proposed by Lattès and Lions (1969). Beginning from a starting guess, an initial condition is reconstructed using a backward energy equation that contains an additional regularization term designed to stabilize diffusion during the back-in-time component of the simulation. The resulting estimate of the initial condition is subsequently run forward in time using the correct energy equation, and the misfit between the final model state and present-day structure is used to update the starting guess. Through a number of iterations (minimum of five; Glišović and Forte, 2019), it is anticipated that the initial condition will improve sufficiently such that it evolves along a pathway that produces a final model state as close as possible to the known present-day state. The original QRV method was introduced within a geodynamical context by Ismail-Zadeh et al. (2007) and has been updated and used to simulate the evolution of mantle flow and its impact at Earth's surface by, for example, Glišović and Forte (2014, 2016) and Faccenna et al. (2019). These studies demonstrate that the approach provides a substantial improvement on the results of backward advection, offering a means to reconstruct key aspects of the mantle's 3D structure and dynamics over the Cenozoic Era that can include the effects of thermal diffusion. Nevertheless, synthetic tests highlight concerns with the accuracy of the QRV approach (Glišović and Forte, 2014), in particular for regions of the mantle that are dominated by diffusion (Ismail-Zadeh and Tackley, 2010; Ismail-Zadeh et al., 2007). This shortcoming is likely a result of introducing the aforementioned regularization term, which will impact diffusive heat transfer during the back-in-time step and ultimately limit the retrievability of the unknown initial condition. As an aside, the QRV studies of Glišović and Forte (2014, 2016) also use a treatment of surface velocity boundary conditions originally developed by Forte and Peltier (1991) — rather than prescribing plate velocities, plate geometries are used to partition underlying forces in such a way that surface velocities are determined using a combination of free-slip and no-slip boundary conditions.

Given the significance of thermal diffusion in dictating structure and dynamics in the shallow mantle, an optimal approach for geodynamical inversion will robustly account for this process. A formal inverse approach, based upon the so-called *adjoint* method, provides a means to accomplish this goal. The method provides a way to globally correct a model with respect to observations that are distributed in space and time using formal adjoint equations that provide sensitivity information, in conjunction with a forward code (e.g., Talagrand, 1997; Tarantola, 1987). Adjoint equations have been derived for incompressible (Bunge et al., 2003; Ismail-Zadeh et al., 2004), compressible (Ghelichkhan and Bunge, 2016), and thermochemical (Ghelichkhan and Bunge, 2018) mantle flow. The method has been used to compute an optimal initial condition for mantle flow that provides a present-day state that is consistent, within observational and epistemic errors, with

seismological observations of the mantle (e.g., Bunge et al., 2003; Colli et al., 2018; Ghelichkhan et al., 2021; Liu and Gurnis, 2008; Liu et al., 2008; Price and Davies, 2018). In contrast to sequential assimilation methods, the adjoint approach propagates information and uncertainties both forwards and backwards in time (Fig. 6C). Furthermore, with the diffusion term in the adjoint energy equation having the opposite sign to that of the forward energy equation, it is unconditionally stable to backward-in-time integration (Bunge et al., 2003).

Despite their promise, the uptake of adjoint methods within the geodynamics community has, so far, been limited. This situation is principally due to: (i) the challenge of developing and implementing adjoint models for nonlinear, time-dependent problems, which are notoriously difficult (e.g., Farrell et al., 2013) — to date, global studies have not utilized the full set of compressible adjoint equations applicable to simulations with strongly varying viscosities, which are essential if we are to resolve the role of lithospheric structure and uppermost mantle flow in controlling dynamic topography; and (ii) the computational expense of running this class of models — they require a sequence of forward and adjoint iterations in order to minimize the misfit between model prediction and observation. Nonetheless, owing to increasing computational resources and algorithmic development, this area of computational geodynamics is rapidly evolving and is set to fundamentally change our understanding of the mantle's thermochemical evolution. It is therefore our view that this approach provides the most promising avenue for accurate reconstructions of dynamic topography through space and time.

3.3 Time-dependent global predictions of dynamic topography

The first global predictions of dynamic topography through space and time were developed by Gurnis (1993). Using a semianalytical approach from Richards and Hager (1984), combined with constraints on the reconstructed location of trenches through time from Scotese and Golanka (1992), this study revealed that a large fraction of Phanerozoic continental flooding could be attributed to dynamic subsidence in the vicinity of active subduction zones. Lithgow-Bertelloni and Gurnis (1997) built on this approach to predict dynamic topography at different stages of the Cenozoic Era, reproducing observed flooding trends in the North American, Australian, and Indonesian regions. Such simulations also formed a key component of the analyses of Lithgow-Bertelloni and Silver (1998), which linked dynamic uplift of the African continent to underlying deep-mantle structure. Although the amplitudes of uplift and subsidence predicted in these simulations is greater than those inferred from stratigraphic constraints, they were influential in demonstrating that, when constrained by reconstructions of trench locations, models of global mantle flow could be used to predict changes in long-wavelength dynamic topography at Earth's surface and, hence, the marine inundation of continents.

Building on these early studies, Bunge et al. (1998, 2002) developed the first global mantle circulation models, using improved constraints on the late Mesozoic and Cenozoic plate motion and subduction history (119 Ma to present) from Lithgow-Bertelloni and Richards (1998). These prescribed tectonic reconstructions organize underlying mantle flow, generating a planform of mantle heterogeneity in which the location and depth of slabs is consistent with those imaged through seismic tomography until mid-mantle depths, thereby directly connecting ancient ocean floors to structures within Earth's interior (Bunge and Grand, 2000). Nonetheless, owing to the limited temporal extent of the plate motion reconstructions incorporated, these simulations were unable to reproduce salient features of imaged structure in the deep mantle, including LLVPs. It should be noted that

time-dependent predictions of dynamic topography from these simulations were not analyzed by Bunge et al. (1998, 2002). However, given the strong sensitivity of long-wavelength dynamic topography to deep-mantle structure, it seems unlikely that predictions of dynamic topography would match available observational constraints.

Over the intervening years, there has been a major effort to improve global plate tectonic reconstructions, extending them further into deep time and quantifying their uncertainties by incorporating an ever-growing body of observational and mathematical constraints (e.g., Gurnis et al., 2012; Merdith et al., 2021; Müller et al., 2008, 2016b, 2019; Seton et al., 2012; Stampfli and Borel, 2002; Tetley et al., 2019; Vérard et al., 2015; Young et al., 2019). More recent mantle circulation models, driven by these enhanced reconstructions, predict a present-day upper-mantle planform that is dominated by strong downwellings in regions of plate convergence. In the mid-mantle, cold downwellings are prominent beneath North America and southeast Asia, while remnants of older subduction are visible above the CMB. These downwellings modulate the location of hot material such that it becomes concentrated beneath Africa and the Pacific Ocean, closely matching the general structure of deep-mantle LLVPs imaged with seismic tomography (e.g., Davies et al., 2012; Flament, 2019; Schuberth et al., 2009). We emphasize that the resemblance between model predictions and seismological constraints would deteriorate if these simulations incorporated unreasonable estimates of the mantle's material properties. Of fundamental importance are: (i) a realistic convective vigor, which controls the length and timescales at which convection operates (e.g., Davies and Davies, 2009; Nerlich et al., 2016); (ii) an increase in viscosity with depth, which exerts a primary control on the sinking velocity of slabs (e.g., Bunge et al., 1996, 2002; Rubey et al., 2017); (iii) a temperature-dependent viscosity, which helps to maintain the coherence of the lithosphere and the morphology of slabs during their descent (e.g., Davies et al., 2012; Flament, 2019); and (iv) compressibility, which modulates the relative temperature and buoyancy of downwelling and upwelling features (e.g., Bunge, 2005; Davies et al., 2012; Flament, 2019; Leng and Zhong, 2008). As confidence has grown that these models capture the distribution of mantle heterogeneity through space and time with sufficient accuracy, they have been used to reveal the role of mantle convection in driving long-wavelength dynamic topography in a number of regions, including North America (Flament et al., 2013), the Arctic region (Shephard et al., 2014), the South Atlantic Ocean (Flament et al., 2015), southeast Asia (Zahirovic et al., 2016), eastern Australia (Müller et al., 2016a), northern Africa (Barnett-Moore et al., 2017), and eastern China (Cao et al., 2018). Globally, such models have been able to reproduce some aspects of long-wavelength subsidence patterns extracted from well data (Rubey et al., 2017), while also providing an excellent match with observations of continental flooding throughout the Cenozoic Era (Müller et al., 2018a), reinforcing conclusions from the seminal study of Gurnis (1993).

It is now generally accepted that mantle circulation models robustly predict the long-wavelength topographic expression of the plate mode of mantle convection (i.e., those components of mantle flow driven by the mantle's upper thermal boundary layer; Davies, 1999). This element includes subsidence in the vicinity of active and recent subduction zones, rebound as the slab descends and its influence on the surface wanes, and broad uplift associated with passive upwelling away from regions of subduction. This class of model has, however, had limited success in explaining dynamic topography changes at smaller spatial and temporal scales (e.g., Müller et al., 2018a; Rubey et al., 2017). Careful studies by, for example, Osei Tutu et al. (2018), Coltice et al. (2018), and Arnould et al. (2018), demonstrate that these

components of dynamic topography are particularly sensitive to rheological assumptions such as yielding in the shallow crust and lithosphere. Such aspects have, thus far, been neglected in global mantle circulation models owing to algorithmic and computational limitations. Furthermore, our analyses of the present-day dynamic topography demonstrate that these components will be sensitive to lithospheric structure and shallow mantle flow, neither of which are well resolved by the current generation of mantle circulation models. Finally, despite some simulations generating primary upwelling mantle plumes in locations that are not inconsistent with expectations from the observational record (e.g., Davies et al., 2015a; Hassan et al., 2016), mantle circulation models have been less successful in resolving the topographic consequences of the plume mode of mantle convection (i.e., those components of mantle flow driven by the lower thermal boundary layer; Davies, 1999). The key reason for this discrepancy is that this class of models does not exploit any direct observational constraints on short- and intermediate-scale upwelling flow, including constraints on the present-day mantle structure from seismological and geodetic observations. As noted in Section 3.2, overcoming this limitation requires an inverse approach.

Using a backward advection scheme, alongside constraints on the present-day mantle structure from seismic tomography, Conrad and Gurnis (2003) were able to connect Cenozoic uplift of the African continent to upwelling flow associated with the underlying deep-mantle LLVP, corroborating the conclusions of Lithgow-Bertelloni and Silver (1998). By exploiting a similar approach, alongside additional constraints from convection-related surface observables, Moucha et al. (2008) concluded that there is likely to be no such thing as a stable continental platform, which has major implications for our understanding of long-term global sea-level change. Although several issues associated with the backward advection approach have been documented in Section 3.2, the first-order conclusions of these studies have stood the test of time. This finding is likely related to the fact that the studies focused on the analysis of long-wavelength features over short temporal durations, where the impacts of erroneous diffusion are less apparent. As noted in Section 3.2, some of the shortcomings of backward advection are overcome by the QRV method, and this is evidenced by the fact that global models by Glišović and Forte (2016) are among the first to produce upwelling plume dynamics that can be closely reconciled with the surface volcanic record (Glišović and Forte, 2017, 2019). The potential for such an approach to capture the topographic consequences of the plume mode of mantle convection is demonstrated by Faccenna et al. (2019), where a long-lived topographic gradient, sustained by upwelling flow beneath Ethiopia and downwelling flow beneath the Levant Sea and northern Egypt, has been invoked to explain the persistence and stability of the Nile river for ~30 Myr. Nonetheless, given concerns with the accuracy of the QRV approach in regions of the mantle dominated by diffusion (e.g., Ismail-Zadeh and Tackley, 2010; Ismail-Zadeh et al., 2007), it is important for future studies to verify these predictions using more formal adjoint schemes as their usage, efficiency, and applicability continues to develop.

The first application of the adjoint approach for global mantle convection was by Liu et al. (2008) and Spasojevic et al. (2009), who focused on reconstructing subduction of the Farallon slab and its impact at Earth's surface over the past 100 Myr. In doing so, they were able to directly link the formation and subsequent disappearance of the Cretaceous interior seaway to underlying mantle flow, reconciling model predictions with many of the observational constraints outlined in Section 3.1 and confirming the hypotheses of Bond (1978b), Cross and Pilger (1978), Mitrovica et al. (1989), and Burgess et al. (1997). An important finding from

these studies was the sensitivity of the scale and temporal duration of subsidence to the mantle's viscosity structure: models deemed consistent with stratigraphic observations could therefore be used to constrain the depth dependence of mantle viscosity. The simulations of Liu et al. (2008) were further analyzed by Shephard et al. (2010), to reveal the key role of dynamic topography in driving Miocene reversal of the Amazon River in South America. Together, these studies were influential in demonstrating the power of adjoint methods for reconstructing the spatial and temporal evolution of dynamic topography. Nevertheless, they suffered from two important shortcomings: (i) a "stress guide" was required to recover the subduction pathway of the Farallon slab, likely owing to the neglection of complex rheologies and interactions that control the evolution of flat-slab subduction (e.g., Garel et al., 2014); and (ii) the adjoint approach was only applied to the energy equation (Liu and Gurnis, 2008) with no coupling to the Stokes and continuity equations.

The latter shortcoming was overcome by Colli et al. (2018), who used the complete adjoint equations for compressible convection to analyze the evolution of dynamic topography in the South Atlantic and African regions. It is reassuring that at long wavelengths, predictions of dynamic topography from Colli et al. (2018) are generally compatible with earlier generations of mantle circulation models, although they also capture intermediate wavelength features associated with the plume mode of mantle convection, including the "basin and swell" morphology of the African continent. Comparing predictions more closely, exemplar mantle circulation models by Rubey et al. (2017) predict dynamic support beneath southern Africa that gradually develops through the Cretaceous period. The models of Colli et al. (2018), however, predict a multistage uplift history, including a substantial post-30 Ma uplift phase, which appears to be more consistent with many of the observational constraints that argue for significant Neogene rejuvenation of African topography (Section 3.1).

The study of Ghelichkhan et al. (2021) was the first to undertake systematic comparisons between adjoint models and observational constraints at the global scale. Ghelichkhan et al. (2021) examined a suite of eight high-resolution adjoint simulations, comprising different combinations of depth-dependent viscosity profiles and estimates of the present-day mantle heterogeneity. Shallow mantle structure (<300 km) is constrained by the SL2013sv surface-wave tomography model (Schaeffer and Lebedev, 2013), which introduces substantially higher resolution features that have previously been absent from most time-dependent studies, while the deeper mantle makes use of two different whole-mantle models (French and Romanowicz, 2015; Simmons et al., 2015). The dynamic topography predictions from one such simulation, RM-μ_1-SL, are next described. The model assumes a present-day deeper mantle structure based on the SEMUCB-WM1 model of French and Romanowicz (2015) and employs the five-layer radial viscosity profile illustrated in Fig. 3B (see Ghelichkhan et al., 2021 for further details).

To allow for straightforward comparison with the observational constraints summarized in Section 3.1, Fig. 7 displays the reconstructed dynamic topography from 50 Ma to the present day in the three continental regions of North America, Australia, and Africa. In the interior of the North American continent (Fig. 7, top row), the model predicts a dynamic topography low to be already present during the early Eocene times that is driven by the downgoing Farallon slab. Much of this negative dynamic topography disappears over the following 20 Myr due to a rebound induced by a combination of the westward drift of North America and continued descent of the slab into the deeper mantle. In addition, the model predicts positive dynamic topography along the eastern margin of North America during the early Eocene,

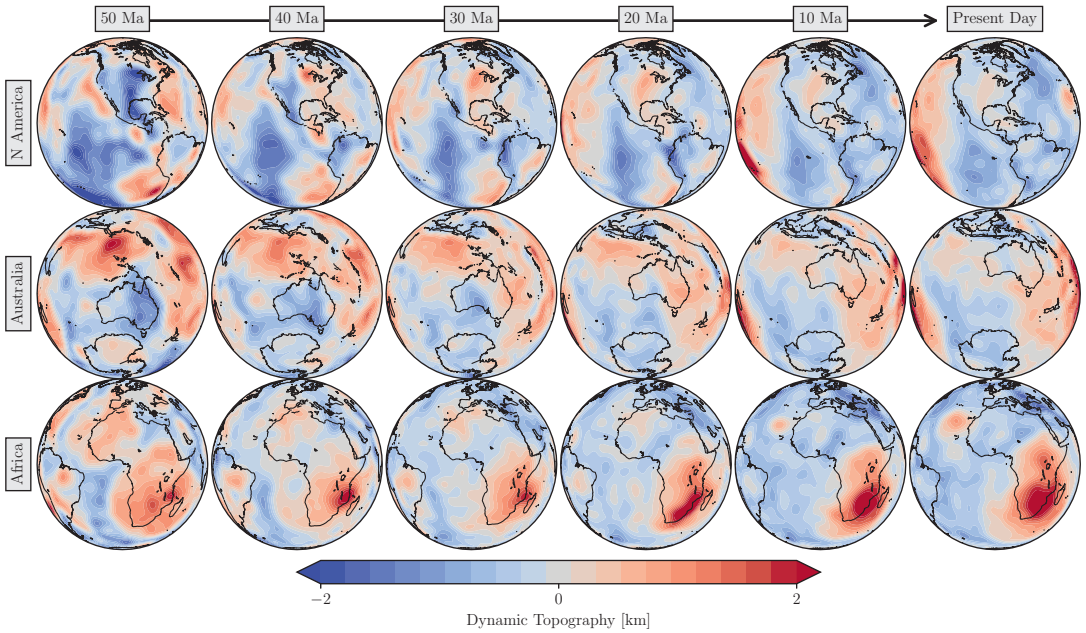

FIG. 7 Air-loaded dynamic topography predictions from the RM-μ_1-SL adjoint simulation of Ghelichkhan et al. (2021) in three regions: *top row* = North America, *middle row* = Australia, and *bottom row* = Africa. Reconstructed coastlines are obtained by back rotation of the present-day coastlines using the plate reconstruction model of Young et al. (2019). See text for further details.

which transitions into negative dynamic topography at the present day. These predictions are broadly consistent with the observed Cenozoic rebound of the Cretaceous interior seaway and also Neogene subsidence recorded in the Baltimore Canyon Trough. Consistent with Liu et al. (2008) and Spasojevic et al. (2009), Ghelichkhan et al. (2021) find a strong sensitivity of dynamic topography predictions to the radial viscosity structure, influencing both the scale and rates at which dynamic topography changes. As will be demonstrated below, they also find a sensitivity to the tomographic model used as a constraint on the present-day mantle density. For North America, however, all eight models consistently predict a dynamic topography low at 50 Ma over the interior of the continent. This general agreement between models is likely related to robust imaging of fast seismic velocity anomalies associated with the Farallon slab in the mantle beneath this region.

Changing focus to Australia (Fig. 7, middle row), the model predicts regional Cenozoic uplift for eastern and southern Australia. This uplift, driven by motion of the Australian plate over the margin of the Pacific LLVP (as suggested by Müller et al., 2016a) has long-wavelength features that are consistent with observations of regional Cenozoic uplift for the continent's central and eastern regions (e.g., Czarnota et al., 2014). It appears after an initial negative signal over much of the continent, which migrates southwards to lie at the AAD at the present day, being driven by the passage of Australia over a relic slab from the Gondwanaland-Pacific convergent margin (Gurnis et al., 1998). The model predicts subsidence in the northern part of the continent in

the late Neogene (shown at 10 Ma), consistent with a range of stratigraphic and geomorphological observations that point toward northward tilting of the continent (e.g., Czarnota et al., 2013; DiCaprio et al., 2009; Sandiford, 2007). Importantly, the Australasian region illustrates the sensitivity of adjoint models to their tomographic input structure — the models of Simmons et al. (2015) and French and Romanowicz (2015) that are used by Ghelichkhan et al. (2021) are less consistent in this region, particularly in the deep mantle, which impacts on regional topographic predictions. This discrepancy highlights the importance of robust tomographic constraints and the key role that they will play in refining future predictions of dynamic topography throughout the Cenozoic Era.

For Africa (Fig. 7, bottom row), model predictions are generally consistent with those of Colli et al. (2018), exhibiting broad uplift over the continent in Eocene times that becomes more localized toward the southern and eastern portions of the continent at the present day. These regions experience a multistage uplift history, culminating with a strong phase of Neogene uplift at rates of $\approx$100 m Myr^{-1}, consistent with, for example, sedimentary flux estimates and regional uplift histories determined from the inversion of river profiles (Section 3.1). In northern Africa, however, a key shortcoming of the models of Ghelichkhan et al. (2021) becomes apparent: the absence of lateral viscosity variations and density anomalies across continental lithosphere contributes to the formation of a large-scale lithospheric drip, which counteracts upwelling flow associated with the African LLVP to drive broad, regional subsidence throughout the Neogene. This pattern is inconsistent with the available observational constraints on dynamic topography in this region, which points toward regional uplift, including the Neogene growth of several shorter-wavelength domes. The neglect of rheological variation across the lithosphere, which is known to facilitate shallow convective processes such as edge-driven convection and shear-driven upwelling (e.g., Conrad et al., 2011; Davies and Rawlinson, 2014; Duvernay et al., 2021; King and Ritsema, 2000; Rawlinson et al., 2017), may also explain why the models of Ghelichkhan et al. (2021) fail to reproduce other aspects of observed dynamic topography at shorter spatial and temporal scales. For example, in North America, the model does not predict localized uplift of the Colorado Plateau in the Neogene — several studies suggest that this uplift is supported by thermochemical buoyancy sources within the lithosphere or shallow asthenospheric flow, which is strongly sensitive to the structure and dynamics of overlying lithosphere (e.g., Afonso et al., 2016; Klöcking et al., 2018). Furthermore, the models do not predict shorter wavelength topographic expressions in the Australian region that are closely associated with step changes in lithospheric thickness (Ball et al., 2021; Davies et al., 2015b), while predicted subsidence rates along the Northwest Shelf since $\sim$10 Ma are lower than those inferred from stratigraphic records (Czarnota et al., 2013; Gurnis et al., 2020). In spite of these limitations, it is important to emphasize that the study of Ghelichkhan et al. (2021) offers one of the most robust modeling constraints on the spatial and temporal evolution of global Cenozoic dynamic topography to date, capturing the topographic consequences of the plate mode of mantle convection and showing promise at resolving shorter wavelength features associated with the plume mode.

3.4 Outlook: Improving dynamic topography reconstructions into the geological past

Observational constraints on dynamic topography become sparser and more patchy deeper into the geological past. The associated geological features can be difficult to interpret, for

example, because transient uplift and subsidence events lead to periodic overprinting of the geological record (Hoggard et al., 2021). Geodynamical simulations of global mantle flow are, therefore, a vital connection between the spatial and temporal evolution of Earth's surface and dynamical processes within its deep interior. Among other things, such simulations provide: (i) a dynamical framework for verifying different, potentially ambiguous, interpretations of the geological record; (ii) insights into the mechanisms controlling dynamic topography at different spatial and temporal scales; and (iii) a means to supplement the observational record where no markers of dynamic topography have been identified.

It is our view that adjoint methods provide the most promising avenue for reconstructing the spatial and temporal evolution of dynamic topography at the global scale. The reasoning behind this, from an algorithmic perspective, has been outlined in Section 3.2: the approach offers a robust mechanism for exploiting diverse observational constraints on the mantle's present-day structure and temporal evolution to guide dynamical simulations that are underpinned by fundamental physical principles. The power of adjoint schemes has been illustrated in Section 3.3: while existing studies have been forced to make some physical simplifications that impact results, they clearly highlight the transformative nature of this approach and its potential to fundamentally improve our understanding of the evolution of dynamic topography across a wide range of spatial and temporal scales.

Nonetheless, the uptake of these schemes within the geodynamics community has been limited, with only a small number of global studies using the approach (Colli et al., 2018; Ghelichkhan et al., 2021; Liu et al., 2008; Shephard et al., 2010; Spasojevic et al., 2009). As noted in Section 3.2, this is principally due to the computational expense of running this class of model, alongside the formidable practical challenges of deriving and implementing adjoints for these problems. In Section 3.3, we introduced a limitation of the models of Ghelichkhan et al. (2021): a rheological approximation that fails to incorporate lateral viscosity variations and yielding in the uppermost mantle. However, extending these models to incorporate more realistic viscoplastic rheologies is a nontrivial task: the nonlinear coupling introduces a number of additional terms in the forward and adjoint equations, the derivation, subsequent implementation, and validation of which is challenging and time consuming. Given these bottlenecks, thus far, global studies have not utilized the full set of compressible adjoint equations relevant for simulations with nonlinear rheologies (e.g., Li et al., 2017). As a result, they are unable to capture a fundamental aspect of uppermost mantle dynamics and its contribution to dynamic topography. Based upon our analyses of the present-day dynamic topography (Section 2), we hypothesize that this shallow mantle contribution is key to explaining the shorter-scale spatial and temporal evolution of dynamic topography, thus explaining why existing models cannot currently be reconciled with all of the available observational constraints.

It is encouraging, therefore, that recent developments in computational sciences promise to open up this class of problem to geodynamical research. High-level finite element software frameworks, such as FEniCS (e.g., Alnes et al., 2014; Logg et al., 2012) and Firedrake (e.g., Rathgeber et al., 2016), allow a user to specify the discrete formulation of a forward model at a high level of mathematical abstraction. State-of-the-art compilers subsequently generate low-level code from these abstractions, incorporating sophisticated performance optimizations that few users would have the resources to code by hand. The combination of these packages with tools that automatically derive a fully consistent adjoint of the discrete equations (e.g., Farrell et al., 2013) offers a radical new approach for the development and use of adjoint-based research software infrastructure, providing a

straightforward mechanism for incorporating different approximations of the governing equations. Demonstrating the applicability of this approach for geodynamical simulation is an ongoing area of research, although the early results are promising (Davies et al., 2022).

Of course, these next-generation tools can only do so much: their success at facilitating reconstructions of dynamic topography in space and time will ultimately be determined by the available observational constraints. Key to successful inverse geodynamic models are tight constraints on the present-day state of the system. Thus far, all global adjoint studies have utilized the present-day constraints on mantle structure from seismic tomography models (e.g., French and Romanowicz, 2015; Schaeffer and Lebedev, 2013; Simmons et al., 2015). As illustrated in Section 3.3 and more completely in the study of Ghelichkhan et al. (2021), predictions of dynamic topography remain strongly sensitive to differences between these tomographic models. The importance of ongoing improvements to tomographic models (e.g., Mousavi et al., 2021; Tkalčić et al., 2015) and a robust estimate of their uncertainty (e.g., Zaroli, 2019), therefore, cannot be overstated. It is also crucial to exploit up-to-date thermodynamic and experimental constraints on density and phase proportions, as well as anelastic corrections, when converting between seismic and physical structure (e.g., Cline et al., 2018; Connolly, 2009; Richards et al., 2020b; Stixrude and Lithgow-Bertelloni, 2005, 2011), tuned to other interdisciplinary geodetic, geodynamic and seismic considerations (e.g., Ghelichkhan et al., 2018; Richards et al., 2020a, b, 2022), and to also account for the uneven resolution inherent to tomographic models (e.g., Bunge and Davies, 2001; Ritsema et al., 2007). Ongoing progress in this area will be fundamental to a successful adjoint model of mantle evolution. Finally, we note that further insight into the present-day mantle structure for future adjoint models can also be derived by combining seismological observations with the complementary constraints from other geodynamical observables, such as the geoid, as advocated by, for example, Moucha et al. (2008) and Glišović and Forte (2016).

While knowledge of the mantle's present-day structure is vital, it provides only limited constraints on the mantle's evolution into the geological past: other observations that extend into the time domain are needed to constrain the time dependence of the system (Fig. 6D). A key constraint comes from the velocity of plates at Earth's surface and the location and nature of plate boundaries (e.g., Colli et al., 2015; Müller et al., 2019). Revealing how tectonic plates and their boundaries have evolved over geological time provides a geographical context that is a prerequisite for understanding how Earth's surface interacts with its interior. As noted in Section 3.3, there have been dramatic improvements in plate tectonic reconstructions over recent years, including extending them into deep time, accounting for lithospheric deformation, and optimizing absolute plate motions in the mantle reference frame (e.g., Merdith et al., 2021; Müller et al., 2019; Tetley et al., 2019). Further developments, including a more robust quantification of uncertainties potentially through the approach of Bocher et al. (2018), will underpin future efforts to reconstruct the evolution of dynamic topography.

A shortcoming of the observational datasets discussed thus far is that they provide only limited constraints on the deep mantle's thermochemical evolution. Among other features of the geological record, geochemical observations from volcanic rocks could potentially help to fill this gap. The principal challenge is to decode these datasets to infer key characteristics of their mantle source (e.g., Davies et al., 2015b; Jones et al., 2017; Niu et al., 2011), since the geochemistry of any melt depends upon source composition, depth, and temperature of melting (e.g., McKenzie and Bickle, 1988). Volcanic rocks

therefore have the potential to provide pointwise constraints on mantle composition and thermal state at specific locations in space and time (e.g., Ball et al., 2019, 2021; Klöcking et al., 2018; McNab et al., 2018), and successfully incorporating these data into future simulations is likely to prove fruitful.

This is an exciting time in geodynamics. With an ever-growing body of high-quality observational constraints on the mantle's thermochemical structure and evolution, alongside ongoing developments in cutting-edge computational algorithms that will provide a framework for fully exploiting these datasets, the stage is set to illuminate the history of our planet's interior in unprecedented detail. Doing so will underpin progress across many areas of geoscience, opening up new possibilities to explore connections between Earth's surface and its interior across a previously unimaginable range of spatial and temporal scales.

Data availability

The specific present-day residual topography dataset used here, which was originally constructed by Hoggard et al. (2017), may be obtained from https://github.com/drhodrid/Davies_etal_NGeo_2019_Datasets. Gaussian process code to analyze the present-day residual topography dataset may be obtained from https://github.com/valentineap/DynamicTopographyGP (https://doi.org/10.5281/zenodo.3895317). Model predictions of dynamic topography and geoid height anomalies may be obtained from https://github.com/drhodrid/Davies_etal_2022_observations_models_dynamic_topography. For full color versions of Fig. 3 refer to https://eartharxiv.org/repository/view/3251.

Acknowledgments

All authors acknowledge support from the Australian Research Data Commons (ARDC: https://ardc.edu.au/, under the G-Adopt platform grant: PL031), AuScope, Geoscience Australia, and the National Computational Infrastructure (NCI). DRD and APV acknowledge support from the Australian Research Council (ARC) (DP200100053). MJH acknowledges support from the Australian Government's *Exploring for the Future* program and an ARC Discovery Early Career Research Award (DE220101519). APV acknowledges an ARC Discovery Early Career Research Award (DE180100040). Numerical simulations were undertaken at the NCI National Facility in Canberra, Australia, which is supported by the Australian Commonwealth Government. The authors are grateful to David Al-Attar, Jacky Austermann, Patrick Ball, Hans-Peter Bunge, Karol Czarnota, Caroline Eakin, Nicolas Flament, Saskia Goes, Marthe Klöcking, Stephan Kramer, Jerry Mitrovica, Dietmar Müller, Nicholas Rawlinson, Malcolm Sambridge, Cian Wilson, Jeff Winterbourne, and many other colleagues for insightful discussions and advice over many years of research on this topic.

References

Afonso, J.C., Rawlinson, N., Yang, Y., Schutt, D.L., Jones, A.-G., Fullea, J., Griffin, W.L., 2016. 3-D multiobservable probabilistic inversion for the compositional and thermal structure of the lithosphere and upper mantle: III. Thermochemical tomography in the Western-Central US. J. Geophys. Res. Solid Earth 121 (10), 7337–7370.

Al-Hajri, Y., White, N.J., Fishwick, S., 2009. Scales of transient convective support beneath Africa. Geology 37 (10), 883–886.

Alnes, M.S., Logg, A., Olgaard, K.B., Rognes, M.E., Wells, G.-N., 2014. Unified form language: a domain-specific language for weak formulations of partial differential equations. ACM Trans. Math. Softw. 40, 2–9.

Arnould, M., Coltice, N., Flament, N., Seigneour, V., Müller, R.D., 2018. On the scales of dynamic topography in whole-mantle convection models. Geochem. Geophys. Geosyst. 19, 1–24. https://doi.org/10.1029/2018GC007516.

Ault, A.K., Flowers, R.M., Bowring, S.A., 2013. Phanerozoic surface history of the Slave Craton. Tectonics 32 (5), 1066–1083.

Austermann, J., Pollard, D., Mitrovica, J.X., Moucha, R., Forte, A.M., DeConto, R.M., Rowley, D.B., Raymo, M.E., 2015. The impact of dynamic topography change on Antarctic ice sheet stability during the mid-Pliocene warm period. Geology 43 (10), 927–930.

Austermann, J., Mitrovica, J.X., Huybers, P., Rovere, A., 2017. Detection of a dynamic topography signal in last interglacial sea-level records. Sci. Adv. 3 (7), e1700457.

Baby, G., Guillocheau, F., Morin, J., Ressouche, J., Robin, C., Broucke, O., Dall'Asta, M., 2018. Post-rift stratigraphic evolution of the Atlantic margin of Namibia and South Africa: implications for the vertical movements of the margin and the uplift history of the South African Plateau. Mar. Pet. Geol. 97, 169–191.

Ball, P.W., White, N.J., Masoud, A., Nixon, S., Hoggard, M.J., Maclennan, J., Stuart, F.M., Oppenheimer, C., Kröpelin, S., 2019. Quantifying asthenospheric and lithospheric controls on mafic magmatism across North Africa. Geochem. Geophys. Geosyst. 20, 3520–3555.

Ball, P.W., Czarnota, K., White, N.J., Klöcking, M., Davies, D.-R., 2021. Thermal structure of Eastern Australia's upper mantle and its relationship to Cenozoic volcanic activity and dynamic topography. Geochem. Geophys. Geosyst. 22 (8). e2021GC009717.

Ballmer, M.D., Houser, C., Hernlund, J.W., Wentzcovitch, R., Hirose, K., 2017. Persistence of strong silica-enriched domains in the Earth's lower mantle. Nat. Geosci. 10, 236–241. https://doi.org/10.1038/NGEO2898.

Barnett-Moore, N., Hassan, R., Müller, R., Williams, S.E., Flament, N., 2017. Dynamic topography and eustasy controlled the paleogeographic evolution of northern Africa since the mid-Cretaceous. Tectonics 36 (5), 929–944.

Barry, T.L., Davies, J.H., Wolstencroft, M., Millar, I.L., Zhao, Z., Jian, P., Safonova, I., Price, M., 2017. Whole-mantle convection with tectonic plates preserves long-term global patterns of upper mantle geochemistry. Sci. Rep. 7 (1), 1–9.

Bishop, P., 1988. The eastern highlands of Australia: the evolution of an intraplate highland belt. Prog. Phys. Geogr. 12 (2), 159–182.

Bocher, M., Coltice, N., Fournier, A., Tackley, P.J., 2016. A sequential data assimilation approach for the joint reconstruction of mantle convection and surface tectonics. Geophys. J. Int. 204, 200–214. https://doi.org/10.1093/gji/ggv427.

Bocher, M., Fournier, A., Coltice, N., 2018. Ensemble Kalman filter for the reconstruction of the Earth's mantle circulation. Nonlinear Proc. Geophys. 25 (1), 99–123. https://doi.org/10.5194/npg-25-99-2018.

Bond, G.C., 1978a. Evidence for late tertiary uplift of Africa relative to North America, South America, Australia and Europe. J. Geol. 86 (1), 47–65.

Bond, G.C., 1978b. Speculations on real sea-level changes and vertical motions of continents at selected times in the cretaceous and tertiary periods. Geology 6, 247–250.

Bond, G.C., 1979. Evidence for some uplifts of large magnitude in continental platforms. Tectonophysics 61, 285–305.

Bower, D.J., Gurnis, M., Flament, N., 2015. Assimilating lithosphere and slab history in 4-D Earth models. Phys. Earth Planet. Inter. 238, 8–22.

Braun, J., 2010. The many surface expressions of mantle dynamics. Nat. Geosci. 3, 826–833. https://doi.org/10.1038/ngeo1020.

Brocher, T.M., 2005. Empirical relations between elastic wavespeeds and density in the Earth's crust. SSA Bull. 95 (6), 2081–2092.

Bunge, H.-P., 2005. Low plume excess temperature and high core heat flux inferred from non-adiabatic geotherms in internally heated mantle circulation models. Phys. Earth Planet. Inter. 153, 3–10. https://doi.org/10.1016/j.pepi.2005.03.017.

Bunge, H.-P., Davies, J.H., 2001. Tomographic images of a mantle circulation model. Geophys. Res. Lett. 28, 77–80.

Bunge, H.-P., Grand, S.P., 2000. Mesozoic plate-motion history below the Northeast Pacific Ocean from seismic images of the subducted Farallon slab. Nature 405 (6784), 337–340.

Bunge, H.-P., Richards, M.A., Baumgardner, J.R., 1996. The effect of depth-dependent viscosity on the planform of mantle convection. Nature 279, 436–438. https://doi.org/10.1038/379436a0.

Bunge, H.-P., Richards, M.A., Lithgow-Bertelloni, C., Baumgardner, J.R., Grand, S., Romanowicz, B., 1998. Time scales and heterogeneous structure in geodynamic Earth models. Science 280, 91–95. https://doi.org/10.1126/science.280.5360.91.

Bunge, H., Richards, M.A., Baumgardner, J.R., 2002. Mantle circulation models with sequential data-assimilation: inferring present-day mantle structure from plate motion histories. Philos. Trans. R. Soc. Lond. Ser. A 360, 2545–2567. 10.1098/rsta.2002.1080.

Bunge, H.-P., Hagelberg, C.R., Travis, B.J., 2003. Mantle circulation models with variational data assimilation: inferring past mantle flow and structure from plate motion histories and seismic tomography. Geophys. J. Int. 152, 280–301. https://doi.org/10.1046/j.1365-246X.2003.01823.x.

Burgers, G., Jan van Leeuwen, P., Evensen, G., 1998. Analysis scheme in the ensemble Kalman filter. Mon. Weather Rev. 126 (6), 1719–1724.

Burgess, P.M., Gurnis, M., 1995. Mechanisms for the formation of cratonic stratigraphic sequences. Earth Planet. Sci. Lett. 136, 647–663.

Burgess, P.M., Gurnis, M., Moresi, L., 1997. Formation of sequences in the cratonic interior of North America by interaction between mantle, eustatic, and stratigraphic processes. GSA Bull. 109 (12), 1515–1535.

Burke, K., Steinberger, B., Torsvik, T.H., Smethurst, M.A., 2008. Plume generation zones at the margins of large low shear velocity provinces on the core-mantle-boundary. Earth Planet. Sci. Lett. 265, 49–60. https://doi.org/10.1016/j.epsl.2007.09.042.

Campbell, S.M., Moucha, R., Derry, L.A., Raymo, M.E., 2018. Effects of dynamic topography on the Cenozoic carbonate compensation depth. Geochem. Geophys. Geosyst. 19, 1025–1034.

Cao, X., Flament, N., Müller, D., Li, S., 2018. The dynamic topography of eastern China since the latest Jurassic Period. Tectonics 37 (5), 1274–1291.

Cao, X., Flament, N., Bodur, Ö.F., Müller, R.D., 2021. The evolution of basal mantle structure in response to supercontinent aggregation and dispersal. Sci. Rep. 11 (1), 1–16.

Carena, S., Bunge, H.-P., Friedrich, A.M., 2019. Analysis of geological hiatus surfaces across Africa in the Cenozoic and implications for the timescales of convectively-maintained topography. Can. J. Earth. Sci. 56 (12), 1333–1346. https://doi.org/10.1139/cjes-2018-0329.

Cazenave, A., Dominh, K., Rabinowicz, M., Ceuleneer, G., 1988. Geoid and depth anomalies over ocean swells and troughs: evidence of an increasing trend of the geoid to depth ratio with age of plate. J. Geophys. Res. 93 (B7), 8064–8077.

Celli, N.L., Lebedev, S., Schaeffer, A.J., Gaina, C., 2020a. African cratonic lithosphere carved by mantle plumes. Nat. Commun. 11 (92), 1–10. https://doi.org/10.1038/s41467-019-13871-2.

Celli, N.L., Lebedev, S., Schaeffer, A.J., Ravenna, M., Gaina, C., 2020b. The upper mantle beneath the South Atlantic Ocean, South America and Africa from waveform tomography with massive data sets. Geophys. J. Int. 221, 178–204. https://doi.org/10.1093/gji/ggz574.

Chambat, F., Ricard, Y., Valette, B., 2010. Flattening of the Earth: further from hydrostaticity than previously estimated. Geophys. J. Int. 183 (2), 727–732.

Chamberlain, C.P., Mix, H.T., Mulch, A., Hren, M.T., Kent-Corson, M.L., Davis, S.J., Horton, T.W., Graham, S.A., 2012. The Cenozoic climatic and topographic evolution of the western north American Cordillera. Am. J. Sci. 312 (2), 213–262.

Chardon, D., Grimaud, J.-L., Rouby, D., Beauvais, A., Christophoul, F., 2016. Stabilization of large drainage basins over geological time scales: Cenozoic West Africa, hot spot swell growth, and the Niger River. Geochem. Geophys. Geosyst. 17, 1164–1181.

Cline, C.J., Faul, U.H., David, E.C., Berry, A.J., Jackson, I., 2018. Redox-influenced seismic properties of upper-mantle olivine. Nature 555 (7696), 355–358.

Cloetingh, S., Gradstein, F.M., Kooi, H., Grant, A.C., Kaminski, M., 1990. Plate reorganization: a cause of rapid late Neogene subsidence and sedimentation around the North Atlantic? J. Geol. Soc. 147 (3), 495–506.

Cochran, J.R., Talwani, M., 1977. Free-air gravity anomalies in the world's oceans and their relationship to residual elevation. Geophys. J. R. Astron. Soc. 50, 495–552.

Coffin, M.F., Duncan, R.A., Eldholm, O., Fitton, J.G., Frey, F.-A., Larsen, H.C., Mahoney, J.J., Saunders, A.D., Schlich, R., Wallace, P.J., 2006. Large igneous provinces and scientific ocean drilling: status quo and a look ahead. Oceanography 19 (4), 150–160.

Colli, L., Bunge, H.-P., Schuberth, B.S.A., 2015. On retrodictions of global mantle flow with assimilated surface velocities. Geophys. Res. Lett. 42, 8341–8348. https://doi.org/10.1002/2015GL066001.

Colli, L., Ghelichkhan, S., Bunge, H.-P., 2016. On the ratio of dynamic topography and gravity anomalies in a dynamic Earth. Geophys. Res. Lett. 43, 2510–2516. https://doi.org/10.1002/2016GL067929.

Colli, L., Ghelichkhan, S., Bunge, H.-P., Oeser, J., 2018. Retrodictions of Mid Paleogene mantle flow and dynamic topography in the Atlantic region from compressible high resolution adjoint mantle convection models: sensitivity to deep mantle viscosity and tomographic input model. Gondwana Res. 53, 252–272. https://doi.org/10.1029/2018GL077338.

Coltice, N., Larrouturou, G., Debayle, E., Garnero, E.J., 2018. Interactions of scales of convection in the Earth's mantle. Tectonophysics 746, 669–677. https://doi.org/10.1016/j.tecto.2017.06.028.

Connolly, J.A.D., 2005. Computation of phase equilibria by linear programming: a tool for geodynamic modeling and its application to subduction zone decarbonation. Earth Planet. Sci. Lett. 236 (1–2), 524–541.

Connolly, J.A.D., 2009. The geodynamic equation of state: what and how. Geochem. Geophys. Geosyst. 10, Q10014.

Conrad, C.P., Gurnis, M., 2003. Seismic tomography, surface uplift, and the breakup of Gondwana land: integrating mantle convection backwards in time. Geochem. Geophys. Geosyst. 4. https://doi.org/10.1029/2001GC000299.

Conrad, C., Husson, L., 2009. Influence of dynamic topography on sea level and its rate of change. Lithosphere 1, 110–120. https://doi.org/10.1130/L32.1.

Conrad, C.P., Lithgow-Bertelloni, C., Louden, K.E., 2004. Iceland, the Farallon slab, and dynamic topography of the North Atlantic. Geology 32 (3), 177–180.

Conrad, C.P., Bianco, T.A., Smith, E.I., Wessel, P., 2011. Patterns of intra-plate volcanism controlled by asthenospheric shear. Nat. Geosci. 4, 317–321. https://doi.org/10.1038/NGEO1111.

Crosby, A.G., McKenzie, D., 2009. An analysis of young ocean depth, gravity and global residual topography. Geophys. J. Int. 178, 1198–1219. https://doi.org/10.1111/j.1365-246X.2009.04224.x.

Crosby, A.G., McKenzie, D.P., Sclater, J.G., 2006. The relationship between depth, age and gravity in the oceans. Geophys. J. Int. 166, 553–573.

Crosby, A.G., Fishwick, S., White, N.J., 2010. Structure and evolution of the intracratonic Congo basin. Geochem. Geophys. Geosyst. 11 (6), Q06010.

Cross, T.A., Pilger, R.H., 1978. Tectonic controls of late Cretaceous sedimentation, western interior, USA. Nature 274, 653–657.

Crough, S.T., 1983. Hotspot swells. Ann. Rev. Earth Planet. Sci. 11, 165–193. https://doi.org/10.1146/annurev.ea.11.050183.001121.

Czarnota, K., Hoggard, M.J., White, N., Winterbourne, J., 2013. Spatial and temporal patterns of Cenozoic dynamic topography around Australia. Geochem. Geophys. Geosyst. 14, 634–658. https://doi.org/10.1029/2012GC004392.

Czarnota, K., Roberts, G.G., White, N.J., Fishwick, S., 2014. Spatial and temporal patterns of Australian dynamic

topography from river profile modelling. J. Geophys. Res. 119, 1384–1419. https://doi.org/10.1002/2013JB010436.
Dahlen, F.A., Tromp, J., 1998. Theoretical Global Seismology. Princeton University Press, Princeton, NJ.
Davaille, A., Romanowicz, B., 2020. Deflating the LLSVPs: bundles of mantle thermochemical plumes rather than thick stagnant "piles". Tectonics 39 (10). e2020TC006265.
Davies, G.F., 1988. Ocean bathymetry and mantle convection: 1. Large-scale flow and hotspots. J. Geophys. Res. 93, 10467–10480. https://doi.org/10.1029/JB093iB09p10467.
Davies, G.F., 1999. Dynamic Earth: Plates, Plumes and Mantle Convection. Cambridge University Press, p. 474.
Davies, D.R., Davies, J.H., 2009. Thermally-driven mantle plumes reconcile multiple hotspot observations. Earth Planet. Sci. Lett. 278, 50–54. https://doi.org/10.1016/j.epsl.2008.11.027.
Davies, D.R., Rawlinson, N., 2014. On the origin of recent intra-plate volcanism in Australia. Geology 42, 1031–1034. https://doi.org/10.1016/j.epsl.2014.11.052.
Davies, D.R., Wilson, C.R., Kramer, S.C., 2011. Fluidity: a fully unstructured anisotropic adaptive mesh computational modeling framework for geodynamics. Geochem. Geophys. Geosyst. 120, Q06001. https://doi.org/10.1029/2011GC003551.
Davies, D.R., Goes, S., Davies, J.H., Schuberth, B.S.A., Bunge, H.-P., Ritsema, J., 2012. Reconciling dynamic and seismic models of Earth's lower mantle: the dominant role of thermal heterogeneity. Earth Planet. Sci. Lett. 353–354, 253–269. https://doi.org/10.1016/j.epsl.2012.08.016.
Davies, D.R., Davies, J.H., Bollada, P.C., Hassan, O., Morgan, K., Nithiarasu, P., 2013. A hierarchical mesh refinement technique for global 3D spherical mantle convection modelling. Geosci. Mod. Dev. 6, 1095–1107. https://doi.org/10.5194/gmd-6-1095-2013.
Davies, D.R., Goes, S., Sambridge, M., 2015a. On the relationship between volcanic hotspot locations, the reconstructed eruption sites of large igneous provinces and deep mantle seismic structure. Earth Planet. Sci. Lett. 411, 121–130. https://doi.org/10.1016/j.epsl.2014.11.052.
Davies, D.R., Rawlinson, N., Iaffaldano, G., Campbell, I.H., 2015b. Lithospheric controls on magma composition along Earth's longest continental hotspot track. Nature 525, 511–514. https://doi.org/10.1038/nature14903.
Davies, D.R., Le Voci, G., Goes, S., Kramer, S.C., Wilson, C.R., 2016. The mantle wedge's transient 3-D flow regime and thermal structure. Geochem. Geophys. Geosyst. 17, 78–100. https://doi.org/10.1002/2015GC006125.
Davies, D.R., Valentine, A.P., Kramer, S.C., Rawlinson, N., Hoggard, M.J., Eakin, C., Wilson, C., 2019. Earth's multi-scale topographic response to global mantle flow. Nat. Geosci. 12, 845–850. https://doi.org/10.1038/s41561-019-0441-4.
Davies, D.R., Kramer, S.C., Ghelichkhan, S., Gibson, A., 2022. Towards automatic finite-element methods for geodynamics via Firedrake. Geosci. Model Dev. 15, 5127–5166.
Davis, M.W., White, N.J., Priestley, K.F., Baptie, B.J., Tilmann, F.J., 2012. Crustal structure of the British Isles and its epeirogenic consequences. Geophys. J. Int. 190, 705–725.
DiCaprio, L., Gurnis, M., Müller, R.D., 2009. Long-wavelength tilting of the Australian continent since the Late Cretaceous. Earth Planet. Sci. Lett. 278, 175–185. https://doi.org/10.1016/j.epsl.2008.11.030.
DiCaprio, L., Müller, R.D., Gurnis, M., 2010. A dynamic process for drowning carbonate reefs on the northeastern Australian margin. Geology 38 (1), 11–14.
DiCaprio, L., Gurnis, M., Müller, R.D., Tan, E., 2011. Mantle dynamics of continent wide Cenozoic subsidence and tilting of Australia. Lithosphere 3 (5), 311–316.
Divins, D.L., 2003. Total Sediment Thickness of the World's Oceans & Marginal Seas. NOAA National Geophysical Data Center, Boulder, CO.
Duvernay, T., Davies, D.R., Mathews, C.R., Gibson, A.H., Kramer, S.C., 2021. Linking intraplate volcanism to lithospheric structure and asthenospheric flow. Geochem. Geophys. Geosyst. 22 (8). e2021GC009953.
Dziewonski, A.M., Anderson, D.L., 1981. Preliminary reference Earth model. Phys. Earth. Planet. Inter. 25, 297–356.
Eakin, C., Lithgow-Bertelloni, C., 2018. An overview of dynamic topography: the influence of mantle circulation on surface topography and landscape. In: Mountains, Climate and Biodiversity. Wiley-Blackwell, pp. 37–50.
Engel, J., Woodhead, J., Hellstrom, J., White, S., White, N., Green, H., 2020. Using speleothems to constrain late Cenozoic uplift rates in karst terranes. Geology 48 (8), 755–760.
Evensen, G., 1994. Sequential data assimilation with a nonlinear quasi-geostrophic model using Monte Carlo methods to forecast error statistics. J. Geophys. Res. Oceans 99 (C5), 10143–10162.
Faccenna, C., Glišović, P., Forte, A., Becker, T.W., Garzanti, E., Sembroni, A., Gvirtzman, Z., 2019. Role of dynamic topography in sustaining the Nile River over 30 million years. Nat. Geosci. 12 (12), 1012–1017.
Farrell, P.E., Ham, D.A., Funke, S.W., Rognes, M.E., 2013. Automated derivation of the adjoint of high-level transient finite element programs. SIAM J. Sci. Comput. 35, C369–C393.
Fernandes, V.M., Roberts, G.G., 2021. Cretaceous to recent net continental uplift from paleobiological data: insights into sub-plate support. GSA Bull. 133, 1217–1236.
Fernandes, V.M., Roberts, G.G., White, N., Whittaker, A.C., 2019. Continental-scale landscape evolution: a history of North American topography. J. Geophys. Res. Earth Surface 124, 2689–2722.
Flament, N., 2019. Present-day dynamic topography and lower-mantle structure from palaeogeographically

constrained mantle flow models. Geophys. J. Int. 216, 2158–2182. https://doi.org/10.1093/gji/ggy526.

Flament, N., Gurnis, M., Müller, R.D., 2013. A review of observations and models of dynamic topography. Lithosphere 5, 189–210. https://doi.org/10.1130/L245.1.

Flament, N., Gurnis, M., Müller, R.D., Bower, D.J., Husson, L., 2015. Influence of subduction history on South American topography. Earth Planet. Sci. Lett. 430, 9–18.

Flament, N., Williams, S., Müller, R., Gurnis, M., Bower, D.J., 2017. Origin and evolution of the deep thermochemical structure beneath Eurasia. Nat. Commun. 8 (1), 1–9.

Flowers, R.M., Schoene, B., 2010. (U-Th)/He thermochronometry constraints on unroofing of the eastern Kaapvaal craton and significance for uplift of the southern African plateau. Geology 38 (9), 827–830. https://doi.org/10.1130/G30980.1.

Flowers, R.M., Shuster, D.L., Wernicke, B.P., Farley, K.A., 2007. Radiation damage control on apatite (U-Th)/He dates from the Grand Canyon region, Colorado Plateau. Geology 35 (5), 447–450.

Forte, A.M., Peltier, R., 1991. Viscous flow models of global geophysical observables: 1. Forward problems. J. Geophys. Res. Solid Earth 96 (B12), 20131–20159.

Frakes, L.A., Burger, D., Apthorpe, M., Wiseman, J., Dettmann, M., Alley, N., Flint, R., Gravestock, D., Ludbrook, N., Backhouse, J., Skwarko, S., Scheibnerova, V., McMinn, A., Moore, P.S., Bolton, B.R., Douglas, J.G., Christ, R., Wade, M., Molnar, R.E., McGowran, B., Balme, B.E., Day, R.A., 1987. Australian Cretaceous shorelines, stage by stage. Palaeogeogr. Palaeoclimatol. Palaeoecol. 59, 31–48.

French, S.W., Romanowicz, B., 2015. Broad plumes rooted at the base of the Earth's mantle beneath major hotspots. Nature, 95–99. https://doi.org/10.1038/nature14876.

Friedrich, A.M., Bunge, H.-P., Rieger, S.M., Colli, L., Ghelichkhan, S., Nerlich, R., 2018. Stratigraphic framework for the plume mode of mantle convection and the analysis of interregional unconformities on geological maps. Gondwana Res. 53, 159–188. https://doi.org/10.1016/j.gr.2017.06.003.

Garel, F., Goes, S., Davies, D.R., Davies, J.H., Kramer, S.C., Wilson, C.R., 2014. Interaction of subducted slabs with the mantle transition-zone: a regime diagram from 2-D thermo-mechanical models with a mobile trench and an overriding plate. Geochem. Geophys. Geosyst. 15, 1739–1765. https://doi.org/10.1002/2014GC005257.

Ghelichkhan, S., Bunge, H.-P., 2016. The compressible adjoint equations in geodynamics: derivation and numerical assessment. GEM Int. J. Geomath. 7 (1), 1–30.

Ghelichkhan, S., Bunge, H.-P., 2018. The adjoint equations for thermochemical compressible mantle convection: derivation and verification by twin experiments. Proc. R. Soc. A 474 (2220), 20180329.

Ghelichkhan, S., Murböck, M., Colli, L., Pail, R., Bunge, H.-P., 2018. On the observability of epeirogenic movement in current and future gravity missions. Gondwana Res. 53, 273–284.

Ghelichkhan, S., Bunge, H., Oeser, J., 2021. Global mantle flow retrodictions for the early Cenozoic using an adjoint method: evolving dynamic topographies, deep mantle structures, flow trajectories and sublithospheric stresses. Geophys. J. Int. 226, 1432–1460. https://doi.org/10.1093/gji/ggab108.

Glišović, P., Forte, A.M., 2014. Reconstructing the Cenozoic evolution of the mantle: implications for mantle plume dynamics under the Pacific and Indian plates. Earth Planet. Sci. Lett. 390, 146–156.

Glišović, P., Forte, A.M., 2016. A new back-and-forth iterative method for time-reversed convection modeling: implications for the Cenozoic evolution of 3-D structure and dynamics of the mantle. J. Geophys. Res. Solid Earth 121 (6), 4067–4084.

Glišović, P., Forte, A.M., 2017. On the deep-mantle origin of the Deccan Traps. Science 355 (6325), 613–616.

Glišović, P., Forte, A.M., 2019. Two deep-mantle sources for Paleocene doming and volcanism in the North Atlantic. Proc. Natl. Acad. Sci. 116 (27), 13227–13232.

Glišović, P., Forte, A.M., Moucha, R., 2012. Time-dependent convection models of mantle thermal structure constrained by seismic tomography and geodynamics: implications for mantle plume dynamics and CMB heat flux. Geophys. J. Int. 190 (2), 785–815.

Goes, S., Agrusta, R., van Hunen, J., Garel, F., 2017. Subduction-transition zone interaction: a review. Geosphere 13, 644–664. 10.1130/GES01476.1.

Grand, S.P., 2002. Mantle shear-wave tomography and the fate of subducted slabs. Philos. Trans. R. Soc. Lond. Ser. A Math. Phys. Eng. Sci. 360, 2475–2491.

Green, P.F., Japsen, P., Chalmers, J.A., Bonow, J.M., Duddy, I.R., 2018. Post-breakup burial and exhumation of passive continental margins: seven propositions to inform geodynamic models. Gondwana Res. 53, 58–81.

Griffiths, R., Campbell, I., 1991. On the dynamics of long-lived plume conduits in the convecting mantle. Earth Planet. Sci. Lett. 103, 214–227. https://doi.org/10.1016/0012-821X(91)90162-B.

Guerri, M., Cammarano, F., Connolly, J.A.D., 2015. Effects of chemical composition, water and temperature on physical properties of continental crust. Geochem. Geophys. Geosyst. 16, 2431–2449.

Guerri, M., Cammarano, F., Tackley, P.J., 2016. Modelling Earth's surface topography: decomposition of the static and dynamic components. Phys. Earth Planet. Inter.

261, 172–186. https://doi.org/10.1016/j.pepi.2016.10.009.

Guillocheau, F., Simon, B., Baby, G., Bessin, P., Robin, C., Dauteuil, O., 2018. Planation surfaces as a record of mantle dynamics: the case example of Africa. Gondwana Res. 53, 82–98.

Guiraud, M., Buta-Neto, A., Quesne, D., 2010. Segmentation and differential post-rift uplift at the Angola margin as recorded by the transform-rifted Benguela and oblique-to-orthogonal-rifted Kwanza basins. Mar. Pet. Geol. 27 (5), 1040–1068. https://doi.org/10.1016/j.marpetgeo.2010.01.017.

Gurnis, M., 1993. Phanerozoic marine inundation of continents driven by dynamic topography above subducting slabs. Nature 364, 589–593. https://doi.org/10.1038/364589a0.

Gurnis, M., Müller, R.D., Moresi, L., 1998. Cretaceous vertical motion of Australia and the Australian-Antarctic discordance. Science 279, 1499–1504.

Gurnis, M., Mitrovica, J.X., Ritsema, J., van Heijst, H.J., 2000. Constraining mantle density structure using geological evidence of surface uplift rates: the case of the African superplume. Geochem. Geophys. Geosyst. 1. 1999GC000035.

Gurnis, M., Yang, T., Cannon, J., Turner, M., Williams, S., Flament, N., Müller, R.D., 2012. Global tectonic reconstructions with continuously deforming and evolving rigid plates. Comput. Geosci. 116, 32–41. https://doi.org/10.1016/j.cageo.2018.04.007.

Gurnis, M., Kominz, M., Gallagher, S.J., 2020. Reversible subsidence on the North West Shelf of Australia. Earth Planet. Sci. Lett. 534, 116070.

Hager, B.H., 1984. Subducted slabs and the geoid: constraints on mantle rheology and flow. J. Geophys. Res. 89, 6003–6015.

Hager, B.H., O'Connell, R.J., 1979. Kinematic models of large-scale flow in the Earth's mantle. J. Geophys. Res. Solid Earth 84 (B3), 1031–1048.

Hager, B.H., Richards, A.M., 1989. Long-wavelength variations in Earth's geoid: physical models and dynamical implications. Philos. Trans. R. Soc. Lond. Ser. A 328, 309–327.

Hager, B.H., Clayton, R.W., Richards, M.A., Comer, R.P., Dziewonski, A.M., 1985. Lower mantle heterogeneity, dynamic topography and the geoid. Nature 313, 541–545. https://doi.org/10.1038/313541a0.

Han, L., Gurnis, M., 1999. How valid are dynamic models of subduction and convection when plate motions are prescribed? Phys. Earth Planet. Inter. 110 (3–4), 235–246.

Hartley, R.A., Roberts, G.G., White, N., Richardson, C., 2011. Transient convective uplift of an ancient buried landscape. Nat. Geosci. 4, 562–565.

Hassan, R., Müller, R.D., Gurnis, M., Williams, S.E., Flament, N., 2016. A rapid burst in hotspot motion through the interaction of tectonics and deep mantle flow. Nature 533 (7602), 239–242.

Hayek, J.N., Vilacís, B., Bunge, H.-P., Friedrich, A.M., Carena, S., Vibe, Y., 2020. Continent-scale hiatus maps for the Atlantic realm and Australia since the upper Jurassic and links to mantle flow induced dynamic topography. Proc. R. Soc. A 476 (2242), 20200390. https://doi.org/10.1098/rspa.2020.0390.

Hillier, J.K., 2010. Subsidence of 'normal' seafloor: observations do indicate 'flattening'. J. Geophys. Res. 115, B03102.

Hillier, J.K., Watts, A.B., 2005. Relationship between depth and age in the North Pacific Ocean. J. Geophys. Res. 110, B02405.

Hoggard, M.J., White, N., Al-Attar, D., 2016. Global dynamic topography observations reveal limited influence of large-scale mantle flow. Nat. Geosci. 9, 456–463. https://doi.org/10.1038/NGEO2709.

Hoggard, M.J., Winterbourne, J., Czarnota, K., White, N., 2017. Oceanic residual depth measurements, the plate cooling model, and global dynamic topography. J. Geophys. Res. 122, 2328–2372. https://doi.org/10.1002/2016JB013457.

Hoggard, M.J., Czarnota, K., Richards, F.D., Huston, D.L., Jaques, A.L., Ghelichkhan, S., 2020. Global distribution of sediment-hosted metals controlled by craton edge stability. Nat. Geosci. 13, 504–510.

Hoggard, M., Austermann, J., Randel, C., Stephenson, S., 2021. Observational estimates of dynamic topography through space and time. In: Mantle Convection and Surface Expressions, American Geophysical Union (AGU), pp. 371–411.

Holdgate, G.R., Wallace, M.W., Gallagher, S.J., Wagstaff, B.E., Moore, D., 2008. No mountains to snow on: major post-Eocene uplift of the East Victoria Highlands; evidence from Cenozoic deposits. Aust. J. Earth Sci. 55 (2), 211–234.

Huntington, K.W., Wernicke, B.P., Eiler, J.M., 2010. Influence of climate change and uplift on Colorado Plateau paleotemperatures from carbonate clumped isotope thermometry. Tectonics 29, TC3005.

Ismail-Zadeh, A., Tackley, P., 2010. Computational Methods for Geodynamics. Cambridge University Press.

Ismail-Zadeh, A., Schubert, G., Tsepelev, I., Korotkii, A., 2004. Inverse problem of thermal convection: numerical approach and application to mantle plume restoration. Phys. Earth Planet. Inter. 145 (1–4), 99–114.

Ismail-Zadeh, A., Korotkii, A., Schubert, G., Tsepelev, I., 2007. Quasi-reversibility method for data assimilation in models of mantle dynamics. Geophys. J. Int. 170 (3), 1381–1398.

Ito, G., Lin, J., Graham, D., 2003. Observational and theoretical studies of the dynamics of mantle plume-mid-ocean ridge interaction. Rev. Geophys. 41 (4), 1017.

Jones, J.G., Veevers, J.J., 1982. A Cainozoic history of Australia's southeast highlands. J. Geol. Soc. Aust. 29, 1–12.

Jones, T., Davies, D., Campbell, I., Iaffaldano, G., Yaxley, G., Kramer, S., Wilson, C.R., 2017. The concurrent emergence and causes of double volcanic hotspot tracks on the Pacific plate. Nature 545, 472–476. https://doi.org/10.1038/nature22054.

Jones, T.D., Maguire, R.R., van Keken, P.E., Ritsema, J., Koelemeijer, P., 2020. Subducted oceanic crust as the origin of seismically slow lower-mantle structures. Prog. Earth Planet. Sci. 7, 1–16.

Kaban, M.K., Schwintzer, P., Artemieva, I.M., Mooney, W.D., 2003. Density of the continental roots: compositional and thermal contributions. Earth Planet. Sci. Lett. 209, 53–69. https://doi.org/10.1016/S0012-821X(03)00072-4.

Kaula, W.M., 1967. Geophysical implications of satellite determinations of the Earth's gravitational field. Space Sci. Rev. 7, 769–794.

King, S.D., Ritsema, J., 2000. African hot spot volcanism: small-scale convection in the upper mantle beneath cratons. Science 290, 1137–1140. https://doi.org/10.1126/science.290.5494.1137.

Klöcking, M., White, N.J., Maclennan, J., McKenzie, D., Fitton, J.G., 2018. Quantitative relationships between basalt geochemistry, shear wave velocity, and asthenospheric temperature beneath western North America. Geochem. Geophys. Geosyst. 19, 3376–3404.

Kominz, M.A., Miller, K.G., Browning, J.V., Katz, M.E., Mountain, G.S., 2016. Miocene relative sea level on the New Jersey shallow continental shelf and coastal plain derived from one-dimensional backstripping: a case for both eustasy and epeirogeny. Geosphere 12 (5), 1437–1456.

Kramer, S.C., Wilson, C.R., Davies, D.R., 2012. An implicit free-surface algorithm for geodynamical simulations. Phys. Earth Planet. Inter. 194, 25–37. https://doi.org/10.1016/j.pepi.2012.01.001.

Kramer, S.C., Davies, D.R., Wilson, C.R., 2021. Analytical solutions for mantle flow in cylindrical and spherical shells. Geosci. Model Dev. 14, 1899–1919. https://doi.org/10.5194/gmd-14-1899-2021.

Lamb, S., Moore, J.D.P., Perez-Gussinye, M., Stern, T., 2020. Global whole lithosphere isostasy: implications for surface elevations, structure, strength, and densities of the continental lithosphere. Geochem. Geophys. Geosyst. 21. e2020GC009150.

Laske, G., Masters, G.A., 1997. A global digital map of sediment thickness. EOS Trans. Am. Geophys. Union 78, F483.

Lattès, R., Lions, J.-L., 1969. The Method of Quasi-Reversibility: Applications to Partial Differential Equations. American Elsevier Pub. Co., New York.

Lau, H.C.P., Mitrovica, J.X., Davis, J.L., Tromp, J., Yang, H.-Y., Al-Attar, D., 2017. Tital tomography constrains Earth's deep-mantle buoyancy. Nature 551, 321–326. https://doi.org/10.1038/nature24452.

Lekic, V., Cottaar, S., Dziewonski, A., Romanowicz, B., 2011. Cluster analysis of global lower mantle tomography: a new class of structure and implications for chemical heterogeneity. Earth Planet. Sci. Lett. 357, 68–77. https://doi.org/10.1016/j.epsl.2012.09.014.

Leng, W., Zhong, S., 2008. Controls on plume heat flux and plume excess temperature. J. Geophys. Res. 113. https://doi.org/10.1029/2007JB005155.

Li, D., Gurnis, M., Stadler, G., 2017. Towards adjoint-based inversion of time-dependent mantle convection with nonlinear viscosity. Geophys. J. Int. 209, 86–105. https://doi.org/10.1093/gji/ggw493.

Lithgow-Bertelloni, C., Gurnis, M., 1997. Cenozoic subsidence and uplift of continents from time-varying dynamic topography. Geology 25 (8), 735–738.

Lithgow-Bertelloni, C., Richards, M.A., 1998. The dynamics of Cenozoic and Mesozoic plate motions. Rev. Geophys. 36, 27–78.

Lithgow-Bertelloni, C., Silver, P.G., 1998. Dynamic topography, plate driving forces and the African superswell. Nature 395, 269–272. https://doi.org/10.1038/26212.

Liu, L., Gurnis, M., 2008. Simultaneous inversion of mantle properties and initial conditions using an adjoint of mantle convection. J. Geophys. Res. Solid Earth 113 (B8).

Liu, L., Spasojevic, S., Gurnis, M., 2008. Reconstructing Farallon plate subduction beneath North America back to the Late Cretaceous. Science 322, 934–938. https://doi.org/10.1126/science.1162921.

Logg, A., Mardal, K., Wells, G., 2012. Automated Solution of Differential Equations by the Finite Element Method: The FEniCS Book. Lecture Notes in Computational Science and Engineering, vol. 84 Springer, Berlin, https://doi.org/10.1007/978-3-642-23099-8.

Lowman, J.P., 2011. Mantle convection models featuring plate tectonic behavior: an overview of methods and progress. Tectonophysics 510 (1–2), 1–16.

MacKay, D., 1992. Bayesian interpolation. Neural Comput. 4, 415–447.

Marquardt, H., Miyagi, L., 2015. Slab stagnation in the shallow lower mantle linked to an increase in mantle viscosity. Nat. Geosci. 8, 311–314. https://doi.org/10.1038/ngeo2393.

Matas, J., Bukowinski, M.S.T., 2007. On the anelastic contribution to the temperature dependence of lower mantle seismic velocities. Earth Planet. Sci. Lett. 259 (1–2), 51–65.

McKenzie, D.P., 1967. Some remarks on heat flow and gravity anomalies. J. Geophys. Res. 72 (24), 6261–6273.

McKenzie, D.A.N., Bickle, M.J., 1988. The volume and composition of melt generated by extension of the lithosphere. J. Petrol. 29 (3), 625–679.

McKeon, R.E., Zeitler, P.K., Pazzaglia, F.J., Idleman, B.D., Enkelmann, E., 2014. Decay of an old orogen: inferences about Appalachian landscape evolution from low-temperature thermochronology. GSA Bull. 126, 31–46.

McLaren, S., Wallace, M.W., Reynolds, T., 2012. The Late Pleistocene evolution of palaeo megalake Bungunnia, southeastern Australia: Q sedimentary record of fluctuating lake dynamics, climate change and the formation of the modern Murray River. Palaeogeogr. Palaeoclimatol. Palaeoecol. 317, 114–127.

McNab, F., Ball, P.W., Hoggard, M.J., White, N.J., 2018. Neogene uplift and magmatism of Anatolia: insights from drainage analysis and basaltic geochemistry. Geochem. Geophys. Geosyst. 19, 175–213.

McNamara, A.K., Zhong, S., 2005. Thermo-chemical structures beneath Africa and the Pacific Ocean. Nature 437, 1136–1139. https://doi.org/10.1038/nature04066.

Menard, H.W., 1969. Elevation and subsidence of oceanic crust. Earth Planet. Sci. Lett. 6, 275–284.

Menard, H.W., 1973. Depth anomalies and the bobbing motion of drifting islands. J. Geophys. Res. 78 (23), 5128–5137.

Merdith, A.S., Williams, S.E., Collins, A.S., Tetley, M.G., Mulder, J.A., Blades, M.L., Young, A., Armistead, S.E., Cannon, J., Zahirovic, S., Müller, R.D., 2021. Extending full-plate tectonic models into deep time: linking the Neoproterozoic and the Phanerozoic. Earth Sci. Rev. 214, 103477. https://doi.org/10.1016/j.earscirev.2020.103477.

Mitrovica, J.X., Jarvis, G.T., 1985. Surface deflections due to transient subduction in a convecting mantle. Tectonophysics 120 (3–4), 211–237.

Mitrovica, J.X., Beaumont, C., Jarvis, G.T., 1989. Tilting of continental interiors by the dynamical effects of subduction. Tectonics 8 (5), 1079–1094.

Molnar, P., England, P.C., Jones, C.H., 2015. Mantle dynamics, isostasy, and the support of high terrain. J. Geophys. Res. 120, 1932–1957. https://doi.org/10.1002/2014JB011724.

Morris, M., Fernandes, V.M., Roberts, G.G., 2020. Extricating dynamic topography from subsidence patterns: examples from Eastern North America's passive margin. Earth Planet. Sci. Lett. 530, 115840.

Moucha, R., Forte, A.M., Mitrovica, J.X., Rowley, D.B., Quere, S., Simmons, N.A., Grand, S.P., 2008. Dynamic topography and long-term sea-level variations: there is no such thing as a stable continental platform. Earth Planet. Sci. Lett. 271, 101–108. https://doi.org/10.1016/j.epsl.2008.03.056.

Mousavi, S., Tkalčić, H., Hawkins, R., Sambridge, M., 2021. Lowermost mantle shear-velocity structure from hierarchical trans-dimensional Bayesian tomography. J. Geophys. Res. Solid Earth 126 (9). e2020JB021557.

Müller, R.D., Sdrolias, M., Gaina, C., Roest, W.R., 2008. Age, spreading rates and spreading asymmetry of the world's ocean crust. Geochem. Geophys. Geosyst. 9. https://doi.org/10.1029/2007GC001743.

Müller, R.D., Flament, N., Matthews, K.J., Williams, S.E., Gurnis, M., 2016a. Formation of Australian continental margin highlands driven by plate-mantle interaction. Earth Planet. Sci. Lett. 441, 60–70. https://doi.org/10.1016/j.epsl.2016.02.025.

Müller, R.D., Seton, M., Zahirovic, S., Williams, S.E., Matthews, K.J., Wright, N.M., Shephard, G.E., Maloney, K.T., Barnett-Moore, N., Hosseinpour, M., Bower, D.J., Cannon, J., 2016b. Ocean basin evolution and global-scale plate reorganization events since Pangea breakup. Annu. Rev. Earth Planet. Sci. 44, 107–138. https://doi.org/10.1146/annurev-earth-060115-012211.

Müller, R., Hassan, R., Gurnis, M., Flament, N., Williams, S.E., 2018a. Dynamic topography of passive continental margins and their hinterlands since the Cretaceous. Gondwana Res. 53, 225–251.

Müller, R.D., Cannon, J., Qin, X., Watson, R.J., Gurnis, M., Williams, S., Pfaffelmoser, T., Seton, M., Russell, S.H.J., Zahirovic, S., 2018b. GPlates: building a virtual earth through deep time. Geochem. Geophys. Geosyst. 19 (7), 2243–2261. https://doi.org/10.1029/2018GC007584.

Müller, R.D., Zahirovic, S., Williams, S.E., Cannon, J., Seton, M., Bower, D.J., Tetley, M.G., Heine, C., Le Breton, E., Liu, S., et al., 2019. A global plate model including lithospheric deformation along major rifts and orogens since the Triassic. Tectonics 38 (6), 1884–1907.

Nerlich, R., Colli, L., Ghelichkhan, S., Schuberth, B.S., Bunge, H., 2016. Constraining central Neo-Tethys Ocean reconstructions with mantle convection models. Geophys. Res. Lett. 43, 9595–9603. https://doi.org/10.1002/2016GL070524.

Niu, Y., Wilson, M., Humphreys, E.R., O'Hara, M.J., 2011. The origin of intra-plate ocean island basalts (OIB): the lid effect and its geodynamic implications. J. Petrol. 52, 1443–1468. https://doi.org/10.1093/petrology/egr030.

Odada, E.O., 1996. Geological evolution of coastal Kenya as inferred from sedimentary sequences and marines terraces. Afr. Geosci. Rev. 3 (3), 1–18.

O'Malley, C.P.B., White, N.J., Stephenson, S.N., Roberts, G.-G., 2021. Large-scale tectonic forcing of the African landscape. J. Geophys. Res. Earth Surf. 126 (12). e2021JF006345.

Osei Tutu, A., Steinberger, B., Sobolev, S.V., Rogozhina, I., Popov, A.A., 2018. Effects of upper mantle heterogeneities on the lithospheric stress field and dynamic topography. Solid Earth 9, 649–668. https://doi.org/10.5194/se-9-649-2018.

Pail, R., Goiginger, H., Schuh, W.-D., Höck, E., Brockmann, J.-M., Fecher, T., Gruber, T., Mayer-Gürr, T., Kusche, J., Jäggi, A., Rieser, D., 2010. Combined satellite gravity field model GOCO01S derived from GOCE and GRACE. Geophys. Res. Lett. 37 (20). https://doi.org/10.1029/2010GL044906.

Panasyuk, S.V., Hager, B.H., 2000. Models of isostatic and dynamic topography, geoid anomalies, and their uncertainties. J. Geophys. Res. 105, 28199–28209. https://doi.org/10.1029/2000JB900249.

Parnell-Turner, R., White, N.J., McCave, I.N., Henstock, T.J., Murton, B., Jones, S.M., 2015. Architecture of North Atlantic contourite drifts modified by transient circulation of the Icelandic mantle plume. Geochem. Geophys. Geosyst. 16 (10), 3414–3435.

Parsons, B., Daly, S., 1983. The relationship between surface topography, gravity anomalies, and temperature structure of convection. J. Geophys. Res. 88, 1129–1144. https://doi.org/10.1029/JB088iB02p01129.

Paul, J.D., Roberts, G.G., White, N., 2014. The African landscape through space and time. Tectonics 33 (6), 898–935.

Pekeris, C.L., 1935. Thermal convection in the interior of the Earth. Geophys. J. 3, 343–367.

Petersen, K.D., Nielsen, S.B., Clausen, O., Stephenson, R., Gerya, T., 2010. Small-scale mantle convection produces stratigraphic sequences in sedimentary basins. Science 329 (5993), 827–830.

Poore, H.R., Samworth, R., White, N.J., Jones, S.M., McCave, I.N., 2006. Neogene overflow of northern component water at the Greenland-Scotland ridge. Geochem. Geophys. Geosyst. 7 (6).

Poore, H.R., White, N., Jones, S., 2009. A Neogene chronology of Iceland plume activity from V-shaped ridges. Earth Planet. Sci. Lett. 283, 1–13. https://doi.org/10.1016/j.epsl.2009.02.028.

Price, M.G., Davies, J.H., 2018. Profiling the robustness, efficiency and limits of the forward-adjoint method for 3-D mantle convection modelling. Geophys. J. Int. 212 (2), 1450–1462.

Rasmussen, C., Williams, C., 2006. Gaussian Processes for Machine Learning. MIT Press, Cambridge, MA.

Rathgeber, F., Ham, D.A., Mitchell, L., Lange, M., Luporini, F., Mcrae, A.T.T., Bercea, G.-T., Markall, G.R., Kelly, P.H.J., 2016. Firedrake: automating the finite element method by composing abstractions. ACT Trans. Math. Softw. 43, 1–24. https://doi.org/10.1145/2998441.

Rawlinson, N., Davies, D.R., Pilia, S., 2017. The mechanisms underpinning Cenozoic intraplate volcanism in eastern Australia: insights from seismic tomography and geodynamic modeling. Geophys. Res. Lett. 44, 9681–9690. https://doi.org/10.1002/2017GL074911.

Ricard, Y., Richards, M.A., Lithgow-Bertelloni, C., LeStunff, Y., 1993. A geodynamic model of mantle mass heterogeneities. J. Geophys. Res. 98, 21895–21909.

Richards, M.A., Hager, B.H., 1984. Geoid anomalies in a dynamic Earth. J. Geophys. Res. 89, 5987–6002.

Richards, F.D., Hoggard, M.J., White, N.J., 2016. Cenozoic epeirogeny of the Indian peninsula. Geochem. Geophys. Geosyst. 17 (12), 4920–4954.

Richards, F.D., Hoggard, M.J., Cowton, L.R., White, N.J., 2018. Reassessing the thermal structure of oceanic lithosphere with revised global inventories of basement depths and heat flow measurements. J. Geophys. Res. 123, 9136–9161. https://doi.org/10.1029/2018JB015998.

Richards, F., Hoggard, M., Crosby, A., Ghelichkhan, S., White, N., 2020a. Structure and dynamics of the oceanic lithosphere-asthenosphere system. Phys. Earth Planet. Inter., 106559.

Richards, F.D., Hoggard, M.J., White, N.J., Ghelichkhan, S., 2020b. Quantifying the relationship between short-wavelength dynamic topography and thermomechanical structure of the upper mantle using calibrated parameterization of anelasticity. J. Geophys. Res. Solid Earth 125. e2019JB019062.

Richards, F., Hoggard, M., Ghelichkhan, S., Koelemeijer, P., Lau, H., 2022. Geodynamic, geodetic, and seismic constraints favour deflated and dense-cored LLVPs. EarthArXiv. https://doi.org/10.31223/X55601.

Ritsema, J., McNamara, A.K., Bull, A., 2007. Tomographic filtering of geodynamic models: implications for model interpretation and large-scale mantle structure. J. Geophys. Res. 112. https://doi.org/10.1029/2006JB004566.

Ritsema, J., Deuss, A.A., Van Heijst, H.J., Woodhouse, J.H., 2011. S40RTS: a degree-40 shear-velocity model for the mantle from new Rayleigh wave dispersion, teleseismic travel time and normal-mode splitting function measurements. Geophys. J. Int. 184 (3), 1223–1236.

Roberts, G.G., White, N.J., 2010. Estimating uplift rate histories from river profiles using African examples. J. Geophys. Res. 2010, B02406.

Roberts, G.G., Paul, J.D., White, N., Winterbourne, J., 2012a. Temporal and spatial evolution of dynamic support from river profiles: a framework for Madagascar. Geochem. Geophys. Geosyst. 13 (4).

Roberts, G.G., White, N.J., Martin-Brandis, G.L., Crosby, A.-G., 2012b. An uplift history of the Colorado Plateau and its surroundings from inverse modeling of longitudinal river profiles. Tectonics 31 (TC4022).

Robinson Roberts, L.N., Kirschbaum, M.A., 1995. Paleogeography of the late Cretaceous of the western interior of middle North America—coal distribution and sediment accumulation. US Geol. Surv. Prof. Paper No. 1561.

Rovere, A., Hearty, P.J., Austermann, J., Mitrovica, J.X., Gale, J., Moucha, R., Forte, A.M., Raymo, M.E., 2015. Mid-Pliocene shorelines of the US Atlantic coastal plain—an improved elevation database with comparison to Earth model predictions. Earth Sci. Rev. 145, 117–131.

Rowley, D.B., Forte, A.M., Moucha, R., Mitrovica, J.X., Simmons, N.A., Grand, S.P., 2013. Dynamic topography change of the eastern United States since 3 million years ago. Science 340 (6140), 1560–1563.

Rubey, M., Brune, S., Heine, C., Davies, D.R., Williams, S.E., Müller, R.D., 2017. Global patterns in Earth's dynamic topography since the Jurassic: the role of subducted slabs. Solid Earth 8, 899–919. https://doi.org/10.5194/se-8-899-2017.

Rudolph, M.L., Lekik, V., Lithgow-Bertelloni, C., 2015. Viscosity jump in Earth's mid-mantle. Science 350, 1349–1352. https://doi.org/10.1126/science.aad4972.

Sahagian, D., 1988. Epeirogenic motions of Africa as inferred from Cretaceous shoreline deposits. Tectonics 7 (1), 125–138. https://doi.org/10.1029/TC007i001p00125.

Said, A., Moder, C., Clark, S., Ghorbal, B., 2015. Cretaceous-Cenozoic sedimentary budgets of the Southern Mozambique Basin: implications for uplift history of the South African Plateau. J. Afr. Earth Sci. 109, 1–10.

Sandiford, M., 2007. The tilting continent: a new constraint on the dynamic topographic field from Australia. Earth Planet. Sci. Lett. 261, 152–163. https://doi.org/10.1016/j.epsl.2007.06.23.

Sandiford, M., Quigley, M., 2009. TOPO-OZ: insights into the various modes of intraplate deformation in the Australian continent. Tectonophysics 474 (1–2), 405–416.

Schaeffer, A.J., Lebedev, S., 2013. Global shear speed structure of the upper mantle and transition zone. Geophys. J. Int. 194, 417–449. https://doi.org/10.1093/gji/ggt095.

Schaeffer, A.J., Lebedev, S., 2014. Imaging the North American continent using waveform inversion of global and USArray data. Earth Planet. Sci. Lett. 402, 26–41. https://doi.org/10.1016/j.epsl.2014.05.014.

Schellart, W.P., Spakman, W., 2015. Australian plate motion and topography linked to fossil New Guinea slab below Lake Eyre. Earth Planet. Sci. Lett. 421, 107–116.

Schuberth, B.S.A., Bunge, H., Steinle-Neumann, G., Moder, C., Oeser, J., 2009. Thermal versus elastic heterogeneity in high-resolution mantle circulation models with pyrolite composition: high plume excess temperatures in the lowermost mantle. Geochem. Geophys. Geosyst. 10, Q01W01. https://doi.org/10.1029/2008GC002235.

Scotese, C.R., Golanka, J., 1992. PALEOMAP Paleogeographic Atlas: PALEOMAP Progress Report No. 20. Department of Geology, University of Texas at Arlington, Arlington, TX, p. 34.

Sembroni, A., Faccenna, C., Becker, T.W., Molin, P., Abebe, B., 2016. Long-term, deep-mantle support of the Ethiopia-Yemen Plateau. Tectonics 35 (2), 469–488.

Seton, M., Müller, R.D., Zahirovic, S., Gaina, C., Torsvik, T., Shephard, G., Talsma, A., Gurnis, M., Turner, M., Maus, S., Chandler, M., 2012. Global continental and ocean basin reconstructions since 200 Ma. Earth Sci. Rev. 113, 212–270. https://doi.org/10.1016/j.earscirev.2012.03.002.

Shephard, G.E., Müller, R.D., Liu, L., Gurnis, M., 2010. Miocene drainage reversal of the Amazon River driven by plate-mantle interaction. Nat. Geosci. 3, 870–875. https://doi.org/10.1038/NGEO1017.

Shephard, G.E., Flament, N., Williams, S., Seton, M., Gurnis, M., Müller, R.D., 2014. Circum-Arctic mantle structure and long-wavelength topography since the Jurassic. J. Geophys. Res. Solid Earth 119 (10), 7889–7908.

Simmons, N.A., Myers, S.C., Johannesson, G., Matzel, E., Grand, S.P., 2015. Evidence for long-lived subduction of an ancient tectonic plate beneath the southern Indian Ocean. Geophys. Res. Lett. 42 (21), 9270–9278. https://doi.org/10.1002/2015gl066237.

Sloss, L.L., 1963. Sequences in the cratonic interior of North America. GSA Bull. 74 (2), 93–114.

Smith, W.H.F., Sandwell, D.T., 1997. Global sea floor topography from satellite altimetry and ship depth soundings. Science 277, 1956–1962.

Spasojevic, S., Gurnis, M., 2012. Sea level and vertical motion of continents from dynamic Earth models since the Late Cretaceous. Am. Assoc. Petrol. Geol. Bull. 10, 2037–2064.

Spasojevic, S., Liu, L., Gurnis, M., 2009. Adjoint models of mantle convection with seismic, plate motion, and stratigraphic constraints: North America since the Late Cretaceous. Geochem. Geophys. Geosyst. 10, 24 pp. https://doi.org/10.1029/2008GC002345.

Stampfli, G.M., Borel, G.D., 2002. A plate tectonic model for the Paleozoic and Mesozoic constrained by dynamic plate boundaries and restored synthetic oceanic isochrons. Earth Planet. Sci. Lett. 196, 17–33.

Stampfli, G.M., Borel, G.D., 2004. The TRANSMED transects in space and time: constraints on the paleotectonic evolution of the Mediterranean domain. In: Cavazza, W., Roure, F., Spakman, W., Stampfli, G.M., Ziegler, P. (Eds.), The TRANSMED Atlas: the Mediterranean region from crust to mantle. Springer Verlag, Berlin, pp. 53–80.

Stanley, J.R., Flowers, R.M., Bell, D.R., 2015. Erosion patterns and mantle sources of topographic change across the southern African Plateau derived from the shallow and deep records of kimberlites. Geochem. Geophys. Geosyst. 16 (9), 3235–3256. https://doi.org/10.1002/2015GC005969.

Steckler, M.S., Watts, A.B., 1978. Subsidence of the Atlantic-type continental margin off New York. Earth Planet. Sci. Lett. 41 (1), 1–13.

Steinberger, B., 2007. Effects of latent heat release at phase boundaries on the flow in the Earth's mantle, phase boundary topography and the dynamic topography at the Earth's surface. Phys. Earth Planet. Inter. 164. https://doi.org/10.1016/j.pepi.2007.04.021.

Steinberger, B., 2016. Topography caused by mantle density variations: observation-based estimates and models derived from tomography and lithosphere thickness. Geophys. J. Int. 205, 604–621. https://doi.org/10.1093/gji/ggw040.

Steinberger, B., O'Connell, R.J., 1998. Advection of plumes in mantle flow: implications for hotspot motion, mantle viscosity and plume distribution. Geophys. J. Int. 132, 412–434.

Steinberger, B., Werner, S.C., Torsvik, T.H., 2010. Deep versus shallow origin of gravity anomalies, topography and volcanism on Earth, Venus and Mars. Icarus 207 (2), 564–577.

Steinberger, B., Conrad, C.P., Osei Tutu, A., Hoggard, M.J., 2019. On the amplitude of dynamic topography at spherical harmonic degree two. Tectonophysics 760, 221–228. https://doi.org/10.1016/j.tecto.2017.11.032.

Stephenson, S.N., Roberts, G.G., Hoggard, M.J., Whittaker, A.C., 2014. A Cenozoic uplift history of Mexico and its surroundings from longitudinal river profiles. Geochem. Geophys. Geosyst. 15, 4734–4758.

Stephenson, S.N., White, N.J., Li, T., Robinson, L.T., 2019. Disentangling intergalcial sea level and global dynamic topography: analysis of Madagascar. Earth Planet. Sci. Lett. 519, 61–69.

Stixrude, L., Lithgow-Bertelloni, C., 2005. Thermodynamics of mantle minerals—I. Physical properties. Geophys. J. Int. 162, 610–632. https://doi.org/10.1111/j.1365-246X.2005.02642.x.

Stixrude, L., Lithgow-Bertelloni, C., 2011. Thermodynamics of mantle minerals—II. Phase equilibria. Geophys. J. Int. 184, 1180–1213. https://doi.org/10.1111/j.1365-246X.2010.04890.x.

Tackley, P.J., 2008. Modelling compressible mantle convection with large viscosity contrasts in a three-dimensional spherical shell using the Yin-Yang grid. Phys. Earth Planet. Inter. 171, 7–18. https://doi.org/10.1016/j.pepi.2008.08.005.

Talagrand, O., 1997. Assimilation of observations, an introduction. J. Met. Soc. Jpn. Ser. II 75 (1B), 191–209.

Tarantola, A.J., 1987. Inverse Problem Theory. Elsevier, New York, NY.

Tetley, M.G., Williams, S.E., Gurnis, M., Flament, N., Müller, R.D., 2019. Constraining absolute plate motions since the Triassic. J. Geophys. Res. 124, 7231–7258. https://doi.org/10.1029/2019JB017442.

Thoraval, C., Richards, M.A., 1997. The geoid constraint in global geodynamics: viscosity structure, mantle heterogeneity models and boundary conditions. Geophys. J. Int. 131 (1), 1–8.

Tkalčić, H., Young, M., Muir, J.B., Davies, D.R., Mattesini, M., 2015. Strong, multi-scale heterogeneity in Earth's lowermost mantle. Sci. Rep. 5 (1), 1–8.

Tolstikhin, I.N., Hofmann, A.W., 2005. Early crust on top of the Earth's core. Phys. Earth Planet. Inter. 148, 109–130.

Trampert, J., Snieder, R., 1996. Model estimations biased by truncated expansions: possible artifacts in seismic tomography. Science 271, 1257–1260.

Turcotte, D.L., Oxburgh, E.R., 1967. Finite amplitude convective cells and continental drift. J. Fluid. Mech. 28 (1), 29–42.

Uluocak, E.Ş., Göğüş, O.H., Pysklywec, R.N., Chen, B., 2021. Geodynamics of East Anatolia-Caucasus domain: inferences from 3D thermo-mechanical models, residual topography, and admittance function analyses. Tectonics. e2021TC007031.

Valentine, A.P., Davies, D.R., 2020. Global models from sparse data: a robust estimate of Earth's residual topography spectrum. Geochem. Geophys. Geosyst. 21 (8). https://doi.org/10.1029/2020GC009240. e2020GC009240.

Valentine, A.P., Sambridge, M., 2018. Optimal regularisation for a class of linear inverse problem. Geophys. J. Int. 215, 1003–1021. https://doi.org/10.1093/gji/ggy303.

Valentine, A., Sambridge, M., 2020a. Gaussian process models—II. Lessons for discrete inversion. Geophys. J. Int. 220, 1648–1656.

Valentine, A.P., Sambridge, M., 2020b. Gaussian process models—I. A framework for probabilistic continuous inverse theory. Geophys. J. Int. 220, 1632–1647.

Vérard, C., Hochard, C., Baumgartner, P.O., Stampfli, G.M., Liu, M., 2015. Geodynamic evolution of the Earth over the Phanerozoic: plate tectonic activity and palaeoclimatic indicators. J. Palaeogeogr. 4 (2), 167–188.

Walford, H.L., White, N.J., Sydow, J.C., 2005. Solid sediment load history of the Zambezi Delta. Earth Planet. Sci. Lett. 238 (1–2), 49–63.

Wang, Y., Liu, L., Zhou, Q., 2022. Topography and gravity reveal denser cratonic lithospheric mantle than previously thought. Geophys. Res. Lett. e2021GL096844.

Watkins, C.E., Conrad, C.P., 2018. Constraints on dynamic topography from asymmetric subsidence of the mid-ocean ridges. Earth Planet. Sci. Lett. 484, 264–275. https://doi.org/10.1016/j.epsl.2017.12.028.

Wellman, P., 1987. Eastern highlands of Australia; their uplift and erosion. BMR J. Aust. Geol. Geophys. 10, 277–286.

Wheeler, P., White, N., 2002. Measuring dynamic topography: an analysis of Southeast Asia. Tectonics 21 (5). 4-1.

White, N., Lovell, B., 1997. Measuring the pulse of a plume with the sedimentary record. Nature 387, 888–891.

Wilson, J.W.P., Roberts, G.G., Hoggard, M.J., White, N.J., 2014. Cenozoic epeirogeny of the Arabian Peninsula from drainage modeling. Geochem. Geophys. Geosyst. 15, 3723–3761.

Winn, C., Karlstrom, K.E., Shuster, D.L., Kelley, S., Fox, M., 2017. 6 Ma age of carving Westernmost Grand Canyon: reconciling geologic data with combined AFT, (U-Th)/He, and $^{4}He/^{3}He$ thermochronologic data. Earth Planet. Sci. Lett. 474, 257–271.

Winterbourne, J.R., Crosby, A.G., White, N.J., 2009. Depth, age and dynamic topography of oceanic lithosphere beneath heavily sedimented Atlantic margins. Earth Planet. Sci. Lett. 287, 137–151.

Winterbourne, J.R., White, N.J., Crosby, A.G., 2014. Accurate measurements of residual topography from the oceanic realm. Tectonics 33, 1–34.

Workman, R.K., Hart, S.R., 2005. Major and trace element composition of the depleted MORB mantle (DMM). Earth Planet. Sci. Lett. 231, 53–72.

Wunsch, C., 1996. The Ocean Circulation Inverse Problem. Cambridge University Press.

Yamauchi, H., Takei, Y., 2016. Polycrystal anelasticity at near-solidus temperatures. J. Geophys. Res. Solid Earth 121 (11), 7790–7820. https://doi.org/10.1002/2016JB013316.

Yang, T., Gurnis, M., 2016. Dynamic topography, gravity and the role of lateral viscosity variations from inversion of global mantle flow. Geophys. J. Int. 207, 1186–1201. https://doi.org/10.1093/gji/ggw335.

Yang, T., Moresi, L., Müller, R.D., Gurnis, M., 2017. Oceanic residual topography agrees with mantle flow predictions at long wavelengths. Geophys. Res. Lett. 44, 10896–10906. https://doi.org/10.1002/2017GL074800.

Young, A., Flament, N., Maloney, K., Williams, S., Matthews, K., Zahirovic, S., Müller, R.D., 2019. Global kinematics of tectonic plates and subduction zones since the late paleozoic era. Geosci. Front. 10 (3), 989–1013. https://doi.org/10.1016/j.gsf.2018.05.011.

Young, A., Flament, N., Hall, L., Merdith, A., 2021. The influence of mantle flow on intracontinental basins: three examples from Australia. Basin Res. 33, 1429–1453.

Zahirovic, S., Matthews, K.J., Flament, N., Müller, R.D., Hill, K.C., Seton, M., Gurnis, M., 2016. Tectonic evolution and deep mantle structure of the eastern Tethys since the latest Jurassic. Earth Sci. Rev. 162, 293–337. https://doi.org/10.1016/j.earscirev.2016.09.005.

Zaroli, C., 2019. Seismic tomography using parameter-free Backus-Gilbert inversion. Geophys. J. Int. 218 (1), 619–630.

Zhang, N., Zhong, S.J., Leng, W., Li, Z.X., 2010. A model for the evolution of Earth's mantle structure since the early Paleozoic. J. Geophys. Res. 115, B06401. https://doi.org/10.1029/2009JB006896.

Zhong, S., McNamara, A., Tan, E., Moresi, L., Gurnis, M., 2008. A benchmark study on mantle convection in a 3-D spherical shell using CitcomS. Geochem. Geophys. Geosyst. 9, Q10017. https://doi.org/10.1029/2008GC002048.